Doctoral Thesis (Abridged)
博士論文（要約）

Targets, mechanisms, and resistance of the translational inhibitor rocaglamide A

（翻訳阻害剤ロカグラミドAの標的、
分子機構、および抵抗性）

Chen Mingming
陳　明明

東京大学大学院新領域創成科学研究科
メディカル情報生命専攻

令和 3 年度
Doctoral Thesis
博士学位論文

Targets, mechanisms, and resistance of the translational inhibitor rocaglamide A
（翻訳阻害剤ロカグラミド A の標的、分子機構、および抵抗性）

2021 年 8 月 5 日
指導教員　岩崎信太郎　主任研究員（理化学研究所）、
客員准教授（東京大学大学院新領域創成科学研究科メディカル情報生命専攻）

Chen Mingming
陳　明明

Table of contents

Targets, mechanisms, and resistance of the translational inhibitor rocaglamide A

1. Introduction

Translation regulation involves multiple steps, including translation initiation, translation elongation, translation termination, and ribosomes recycling (*1*). However, most of the regulation occurs in the first stage of translation, translation initiation (*2*).

1.1. Translation initiation

During translation initiation, the main task incorporates preparation and recognition of the start codon AUG. However, the step of translation initiation remarkably differs in prokaryotes and eukaryotes. In bacteria, the 16S rRNA of 30S ribosomal subunit complementarily binds to the upstream Shine-Dalgarno (SD) sequence before start codon, which therefore recruits 30S ribosomal subunit and prepares for subsequent translation initiation (*3, 4*). In eukaryotes, the initiation of translation is more complex. It relies on a mechanism called scanning (**See Figure 1.1**), where pre-initiation complex (PIC) containing small ribosomal subunit 40S and Met-tRNA scans the 5' untranslated region (5' UTR) until encountering start codon AUG (*5, 6*).

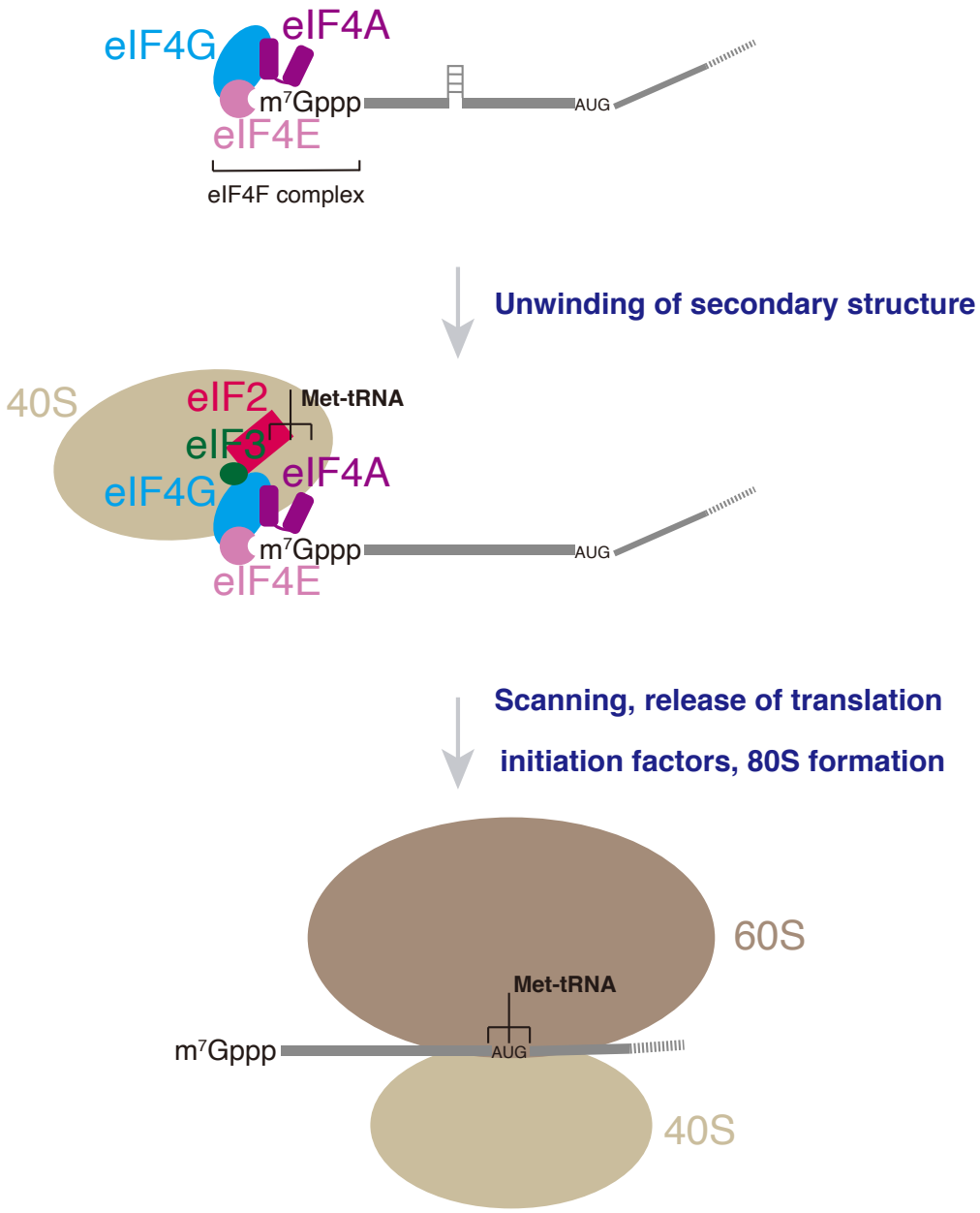

Figure 1.1. Overview of translation initiation.

On the road to learning translation in eukaryotes, enormous efforts have been made to uncover the molecular mechanisms of translation initiation in eukaryotic cells. The high-resolution structure of ribosomal complexes involving eukaryotic translation initiation factors (eIFs) greatly harnessed the progress of identifying critical domains for translation initiation (*5, 7*). In addition, reconstituted translation systems, classical biochemical and genetics assays furtherly decipher the significance of specific factors (*2, 8, 9*). Based on that, the initiation step of

translation was indicated to contain several essential reactions, including placing start codon AUG into the P (peptidyl) decoding center of ribosomes and recruitment of PIC containing Met-tRNAi (initiation tRNA) and eIF1, eIF1A, eIF2, eIF3, and eIF5 into 5′ cap of mRNA. Furthermore, the step of recruitment could be accelerated by eIF4F complexes containing the helicase eIF4A, the large "scaffold" protein eIF4G, and the cap-binding protein eIF4E (*5, 7, 10*).

Once the assembly and recruitment of PIC are completed, the incorporated Met-tRNAi in PIC was ready to recognize the AUG start codon. Therefore, Met-tRNAi is bounded with PIC through eIF2 and inspected triplets along the 5′ end of mRNA until it encounters AUG. With the recognition of the start codon by matching Met-tRNAi to AUG, the hydrolysis of GTP in the complex of eIF2-GTP-Met-tRNAi is arrested. Subsequently, the GTP-hydrolyzed form of eIF2, eIF2-GDP, is released. As a result, the large ribosomal subunit 60S joins with small subunit 40S and forms 80S complex, which can conjugate aminoacyl-tRNAs into A-site (Aminoacyl site) of ribosomes, encode RNA sequences downstream of the start codon, and synthesize the first bond of peptide (*5-7, 10-14*).

For many years, a wealth of studies has carried forward the understanding of translation initiation-related factors (*5-7, 10-14*). For example, eIF1 was indicated to cooperate with eIF1A to promote scanning of 5′ UTR in unstructured mRNAs and facilitate scanning non-AUG codons which occupied ribosomal P-site (*15-20*). As a component of eIF4F, eIF4E binds to the cap from the resolved structure, and the interaction between eIF4G and eIF4E enhances the affinity between eIF4E and the cap of mRNAs (*21, 22*). Besides eIF4E, another component of eIF4F, eIF4A, can unwind the complex secondary structure ahead of PIC scanning by interacting with eIF4G (*23-25*). In addition, as an essential component of PIC, eIF2 not only

functions in basic scanning, but its phosphorylation is also regarded as a hallmark of the integrated stress response (ISR). Upon a widespread of stresses, the α subunit of eIF2 is phosphorylated at Ser^{51}, transforming eIF2 from an activator into an inhibitor of its guanine nucleotide exchange factor (GEF) eIF2B, as a response, leading to a downstream translation deficiency called ISR (*26, 27*).

1.2. Translation initiation is related to cancer development

Given most translation regulation occurs during translation initiation and the overexpression of translation initiation factors is prevalent in multiple types of tumors, the dysregulation of translation initiation often links to human cancers (*5, 10, 11, 13, 14*). For example, as one of the most frequently activated oncogenes, the transcription factor MYC is characterized to coordinate with eIF4F to upregulate the expression of each other, implying the capacity to control MYC by inhibiting eIF4F activity (*28*). More importantly, eIF4F assembly is controlled by the mammalian target of rapamycin (mTOR). Its disturbance is often linked to cancer development (*29, 30*). Overall, targeting the eIF4F components suggests a potential to treat cancers, and considerable evidence has suggested the growth of cancer cells can be suppressed by targeting eIF4F components as eIF4E or eIF4A (*11*).

More broadly, eIF4A belongs to the DEAD-box family (proteins contain the amino acid sequence D-E-A-D (asp-glu-ala-asp)), which shares a conserved structure and is associated with almost all RNA-related processes from RNA transcription to translation (*31-33*). Except eIF4A is known to function in unwinding RNA-duplex structures of the 5′ end of eukaryotic mRNAs and recruitment of 40S ribosome subunits (*24*), the other DEAD-box protein DDX3 has been indicated to play essential roles in the stage of translation initiation as well (*34, 35*).

In general, the functionality of the DEAD-box proteins can be explained as ATPase activity and unwinding activity. The ATPase activity of DEAD-box proteins relies on the stimulation upon ATP binding and RNA binding. In addition, regarding unwinding activity, the contact size between DEAD-box helicases and RNA is typically around 5-6 bp, which step also highly requires ATP-binding (*33, 36-38*).

1.3. Targeting translation initiation factors presents anti-cancer potentials

Given the requirement of translation initiation in maintaining homeostasis, and its frequently aberrant modulation in cancer cells, targeting translation initiation is a promising strategy to treat cancers (*39*). Thus, combined with the prevalent targeting eIF4F-components showing anti-cancer prospects (see section 1.2), many studies have focused on looking for anti-cancer molecules by targeting eIFs.

Targeting eIF4E can date back to the late 1970s. Many cap- analogs represented by Ribavirin were tested for affecting eIF4E-cap binding, but these analogs failed to present any efficiency in cells because of the poor cell permeability (*11, 40*). Following Ribavirin, several drugs were developed for improving their permeability into cells. Among them, 4Ei-1 was proved as an effective drug to kill cancer cells (*41*). After that, inhibitors like 4EGI-1, 4E1RCat, and 4E2RCat showed the capability of inhibiting cancer cell growth. Beyond that, antisense oligonucleotides (ASOs) against eIF4E were also developed and tested in cancer cells and xenograft models (*42*). Because of the promising therapy activities for these ASOs, one of them, ISIS EIF4E Rx, was under clinical trial for killing cancer cells (*42, 43*).

In the high-throughput screening to discover eIF4A inhibitors, several natural molecules such as pateamine A (Pat A), hippuristanol, and silvestrol were found to bind with eIF4A (44-46) selectively. Among these inhibitors, hippuristanol can reduce the affinity between eIF4A and RNAs, whereas Pat A and silvestrol can release eIF4A from eIF4F complexes and force an engagement between eIF4A and RNAs (*44-48*). More recently, the capacity of eIF4A-targeting small molecules was expanded to several new drugs, including Elatol (*49*), Elisabatin A (Elis. A) (*50*), Sanguinarine (SAN) (*51*), 15d-PGJ2 (*52*), and 6-α-aminocholestanol (6-AC) (*53*). Of the above eIF4A inhibitors, the rocaglates that silvestrol belongs to were relatively well-studied and attracted the most attention due to their good pharmacological properties (*54*).

1.4. Rocaglates have anti-cancer potentials

Rocaglates are derived from the plant *Aglaia* genus as secondary metabolites. The members of the *Aglaia* genus consist of about 130 species and spread from Sri Lanka and India, east to the Pacific through Burma, southern mainland China, Taiwan, Vietnam, Malaysia, Indonesia, the Philippines, New Guinea, Northern Australia, and the Western Pacific (*55*). Back in the 1980s, the very first rocaglamide was reported from *A. elliptifolia*. Up to date, around 60 rocaglate derivatives with the cyclopenta[b]benzofurans **(See Figure 1.4.1)** being of the chemical structure were isolated and modified with chemical substitutions in the phenyl ring of their chemical structure (*55, 56*).

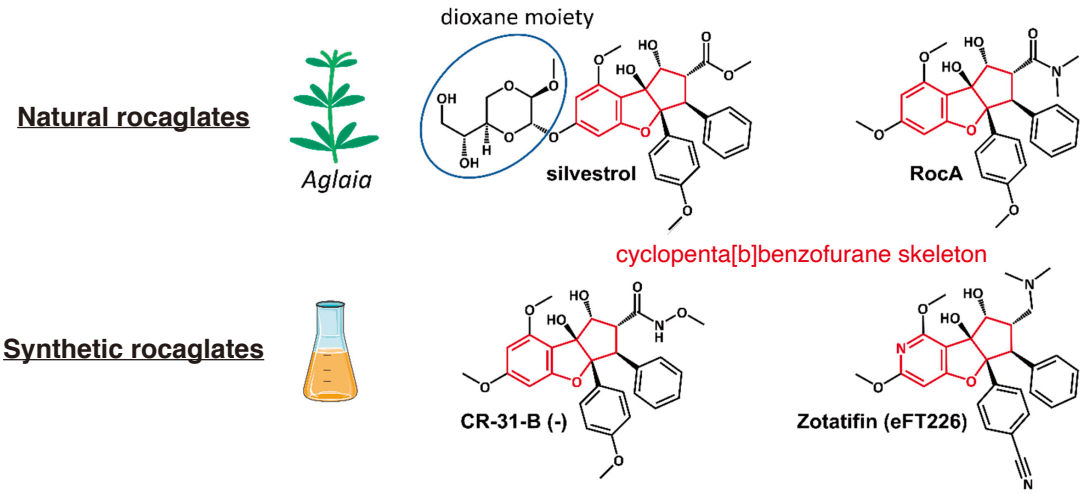

Figure 1.4.1. Examples of rocaglates include natural rocaglates: silvestrol and RocA, and synthetic rocaglates: CR-31-B (-) and Zotatifin (eFT226). The common skeleton cyclopenta[b]benzofurane is highlighted as red. The unique dioxane moiety of silvestrol is highlighted by blue ring. Modified from Taroncher-Oldenburg *et al.* 2021. Microorganisms (*56*).

A pioneering study exploring the cellular mechanisms of rocaglates was published in 2008, in which rocaglates derivative silvestrol was found to be capable of targeting eIF4A (*45*). Another study with a screening of more than 300,000 chemicals revealed that rocaglates could also inhibit HSF1 activation, a gene crucial for tumor development because of its involvement in glucose uptake (*57*). Follow-up mechanistic studies were conducted for several selected rocaglates, some of which were documented to function at the cellular level, including targeting PHBs (*58*), MAPK (*59*), microRNA-155(*60*), as well as FLT3 (*55, 60*). These fundamental studies built a foundation for potentially developing rocaglates as potent anti-cancer drugs. Although extensive efforts and scientific attention have been attracted to explore the therapy potentials against several diseases, the very classical rocaglate, silvestrol, showed poor drug-like properties, bulky structure, and insufficient oral availability (*61*). Consequently, the application of silvestrol as an anti-cancer drug was suspended. Alternatively, other rocaglates instead of silvestrol were evaluated. The study comparing rocaglates lacking the dioxanyl ring of silvestrol indicated that rocaglamide exhibited a practical anti-tumor effect by arresting cell

cycle to G2/M phase through reducing Cdc2's and Cdc25C's expression in cells (*62, 63*). Instead of silvestrol, another commonly used rocaglates with light structure: rocaglamide A (RocA), also attracted significant attention, which was proved to be an effective inhibitor that could selectively kill aneuploid tumor cells by inhibiting the translation of specific messenger RNAs (*57, 64-66*). More recently, as one of the most frequently mutated oncogenes found in pancreatic, lung, colon cancers, and NSCLC, KRAS was reportedly targeted by rocaglate flavagline (*67*). KRAS targeting by flavagline furtherly indicates rocaglates' potential as anti-tumor drugs by inhibiting the oncogenic growth of KRAS-mutated cancer cells. Also, it would be promising to develop the derivatives of flavagline as more potent KRAS inhibitors in clinical applications.

Up to date, the synthesized derivatives, amidino-rocaglates, were proved to be a more potent anti-cancer agent (*68*). More significantly, a synthetic derivative of rocaglates eFT-226 (or Zotatifin, **also see Figure 1.4.1)** is under clinical trial for treating COVID-19 (https://clinicaltrials.gov/ct2/show/study/NCT04632381?cond=zotatifin&draw=2&rank=1) and selected advanced solid tumor malignancies (Phase 1-2, https://clinicaltrials.gov/ct2/show/NCT04092673?cond=zotatifin&draw=2&rank=2), because of its excellent pharmacokinetics in drug development (*69*). After that, extensive follow-up works were done for rocaglates' antineoplastic and antiviral effects. For instance, synthesized aglaroxin C exhibits a weak inhibitory effect on HCV replication (*70*), and rocaglamide shows an inhibitory effect on EV-71 loading (*71*). Recently, the potential neuroprotective effect of the extract from *Aglaia* genus *A. odorata* was also evaluated, while further phytochemical work was still required (*72*).

Given the significant therapy potentials, tremendous efforts have been made to clarify the molecular mechanisms of rocaglates. For example, a fundamental work done with rocaglamide A (RocA) indicated that RocA could liberate eIF4A from eIF4F complexes and convert it into a sequence selective inhibitor by blocking the scanning of PIC (*73*) **(See Figure 1.4.2).** This study also suggested this sequence-selective binding is ATP-independent regardless of the fundamental ATP-dependency of eIF4A. More recently, the understanding of rocaglates' mechanisms was extended to other two actions: 1) trapping the eIF4F complexes onto the cap structure of mRNA; and 2) sequester effect after the resident time of eIF4F extended (*74*), which study is suggesting the hidden complexities of rocaglates.

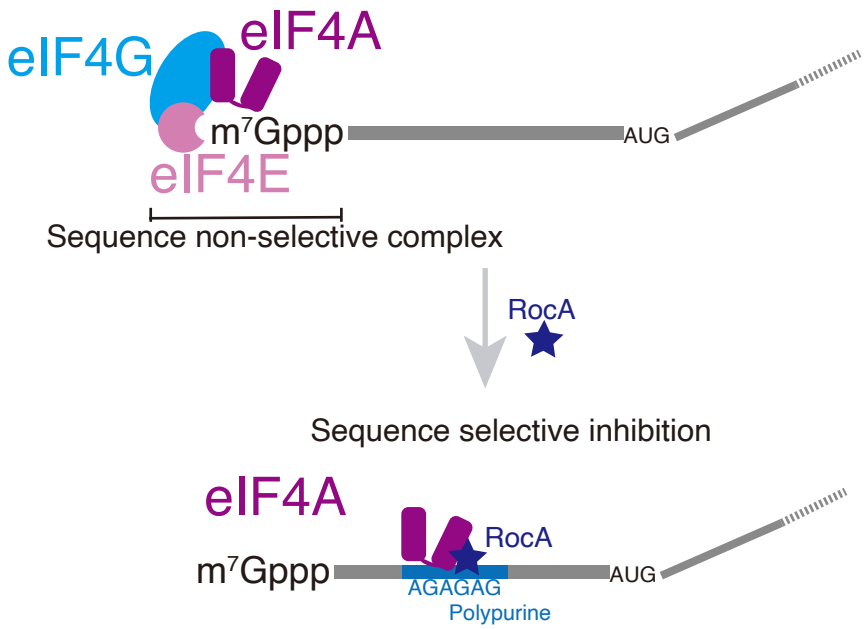

Figure 1.4.2. RocA converts eIF4A into sequence-selective binding.

1.5. Understanding RocA's functionality is a demanding task

Although the progress made to understand rocaglates, there are remaining questions for clearly clarifying the mechanisms of rocaglates. For example, RocA-treated cells do not simply phenocopy the inactivation of eIF4A and exert enhanced repression with the complement of eIF4A. More interestingly, the desensitization of eIF4A to RocA *in cellulo* only rescues cell viability to a limited but not perfect level, suggesting rocaglates might target other alternative targets than eIF4A **(See more details in section 2.1.1)**. Thus, even RocA's targeting to eIF4A has been relatively studied well, exploration of other alternative targets was required.

Except for the lack of investigation for rocaglates' alternative targets, the cause of significantly different sensitivity of cancer cells to rocaglates is still unclear. In a study characterizing the effects of rocaglates on cancer cells, some specific cell lines with highly aneuploid karyotypes were evaluated more sensitive to rocaglates. Taking one of the most potent compounds, RHT, as an example, cancer cells showed an enormous dimension to sense this rocaglate (*57*). However, **why different types of cancer cells sense rocaglates differently remains further clarified**. To solve this question would provide clinical guidance for the usage of the drug.

Moreover, given plenty of natural rocaglates derived from the plant *Aglaia* genus and the indispensable role of their target eIF4A for all eukaryotic species, including plants, the resistance of *Aglaia* to these rocaglates deserves more exploration. In 2019, Iwasaki *et al.* reported a quaternary structure consisting of RocA, human eIF4A1, ATP analog AMP-PNP, and polypurine RNA. They showed that RocA binds to an interface formed between eIF4A1 and polypurine RNAs. Also, in the eIF4A1 cavity that RocA binds to harbors several critical

residues, including Phe163, Gln195, Asp198, and Ile199 (*75*), some of these residues (Phe163, Ile199) were also substituted by specific residues (Phe163 with Leu, Ile199 with Methionine) from the *de novo* assembled *Aglaia* transcriptome. Consistent with this finding, earlier genetic screening of yeast (*61*) and mammalian cell mutagenesis (*76*) have identified Phe163 with Leu in eIF4A could also lead to rocaglates' resistance **(See Figure 1.5)**.

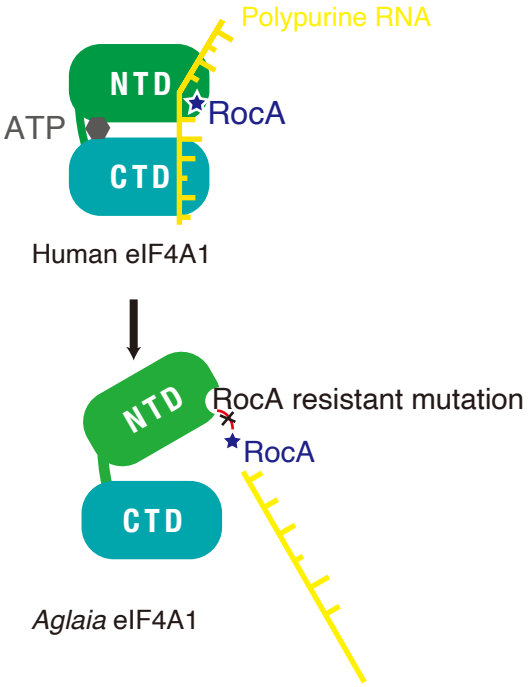

Figure 1.5. *Aglaia* eIF4A1 abolishes RocA's binding by residues' substitutions in RocA's binding pocket.

Considering the structural similarity of DEAD-box proteins in all eukaryotes, and the possibility that RocA alternatively targets multiple proteins besides eIF4A, clarifying if there are any resistance mechanisms of RocA not only for eIF4A would be beneficial and make **it a demanding task to understand how RocA functions comprehensively.**

What's more, given the plant is one of the main hosts of parasites, and parasites like fungi are of great importance regarding their tight relationship with crop health, thus economic loss (*77,*

78). Therefore, underlying plant-fungal interactions and investigating potential anti-fungal drugs have already been extensively studied (*79*). Interestingly, some fungi could overcome the toxic compounds and infect plants. Basically, the standard strategy is detoxification of the antifungal compounds by secreting specific enzymes (*80-82*). Thus, plants and infectious fungi should engage in an arms race during evolution. However, other than the "detoxification", the mechanistic diversity of the plant-fungal competitions centered on plant secondary metabolites is largely uninvestigated. Based on a preliminary observation in our lab that some fungi can coexist with the *Aglaia* plant, I assumed rocaglates and its host *Aglaia* share a specific relationship to live up with each other, so I also sought to clarify the mechanisms of this fungi's resistance to RocA.

To do so, I am looking to understand the functional mechanisms of RocA from the following aspects:

1) Searching for other alternative targets of RocA in addition to eIF4A.
2) Understanding the RocA's mechanisms comprehensively.
3) Clarify how *Aglaia* resists RocA's toxicity.
4) Exploring the reason for the coexistence of *Aglaia* and its parasite fungi.

2. Results I: Dual targeting of DDX3 and eIF4A by RocA

2.1. Targeting of RocA

2.1.1. RocA-*O*-NBD enables the visualization of RocA targets

To investigate other possible targets of RocA besides eIF4A, I initially aim to exclude the disturbance of its known target eIF4A. Also, because there are two paralogs of eIF4A1 and eIF4A2 with approximately 90% of sequence similarity (*23*), they are apparently targeted by RocA **(Figure 2.1.1.1**), which was also validated by fluorescence polarization test **(Also see Figure 2.1.1.1)**.

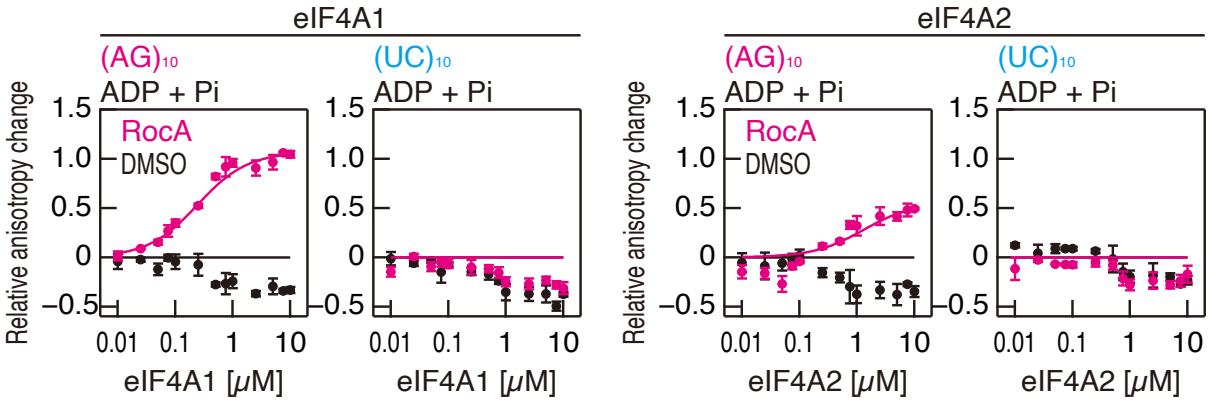

Figure 2.1.1.1. Fluorescence polarization test between eIF4A1/eIF4A2 and polypurine ($(AG)_{10}$) or polypyrimidine ($(UC)_{10}$) RNAs in the presence of ADP + Pi.

To desensitize eIF4A to RocA in cells for investigating other alternative targets, I used a previous HEK293 cell line in which endogenous eIF4A1 was knocked out by CRISPR-Cas9, but an exogenous eIF4A1 with RocA-resistant mutations (Phe163Leu-Ile199Met) was simultaneously expressed [HEK293 SBP-eIF4A1 (Phe163Leu-Ile199Met) *eIF4A1*^{em1SINI}] (*75*)

(Figure 2.1.1.2). As to eIF4A2, I used eIF4A2 siRNA to knock down eIF4A2 from HEK293 SBP-eIF4A1 (Phe163Leu-Ile199Met) *eIF4A1*^{em1SINI} and finally got a cell line with limited RocA-eIF4A targeting. After treating the above cell line with RocA, the cell viability was tested for evaluating the probabilities of other RocA alternative targets besides eIF4A1 and eIF4A2. When RocA-resistant eIF4A1 replaced eIF4A1 in this cell line, and eIF4A2 was knocked down to a minimal level **(Figure 2.1.1.3-A)**, the cell viability from RocA was increased but not completely **(Figure 2.1.1.3-B)**, indicating there must be other targets of RocA.

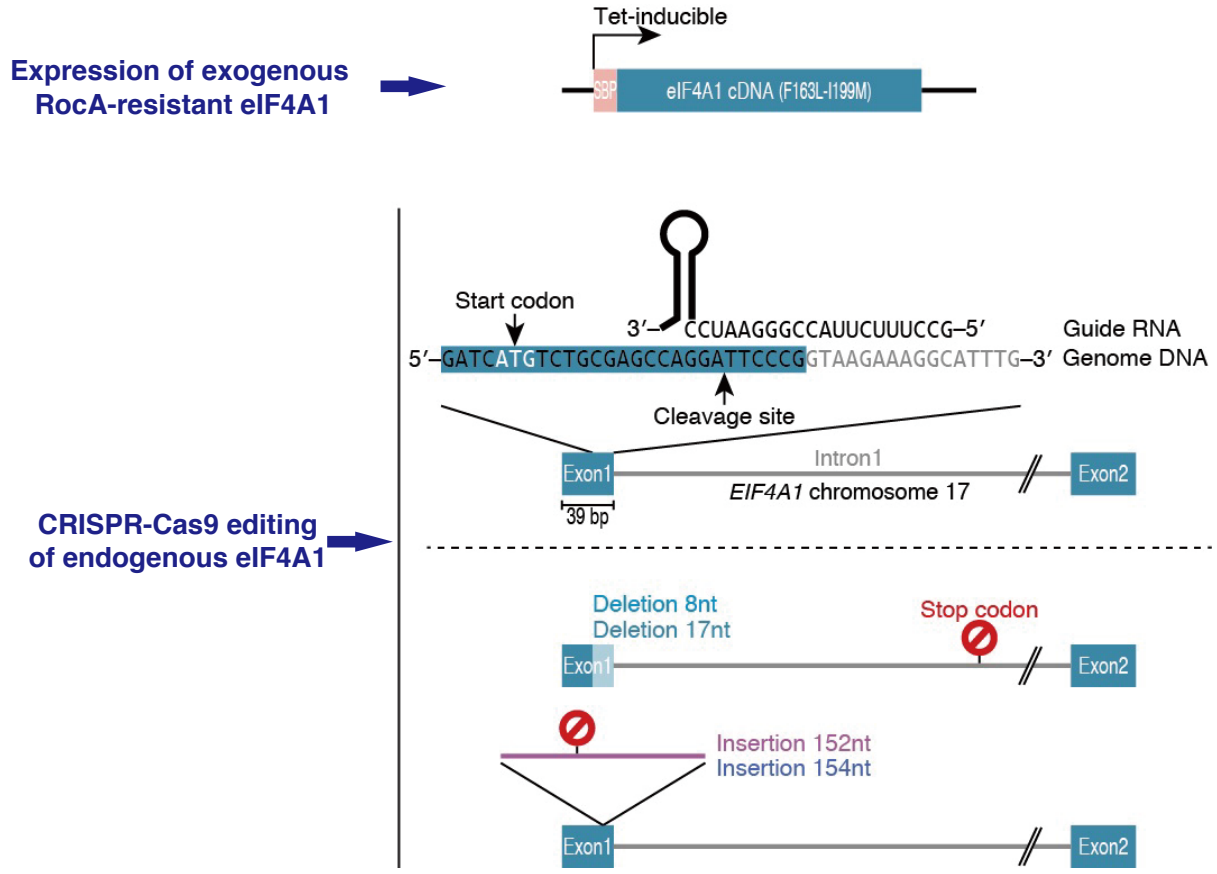

Figure 2.1.1.2. Construction of RocA-resistant eIF4A1 cells, in which exogenous RocA-resistant eIF4A1 (eIF4A1 F163L-I199M) was induced by Tet-induced cDNA, and endogenous eIF4A1 was knocked out by CRISPR-Cas9. Modified from Iwasaki *et al.* 2019. Mol Cell (*75*).

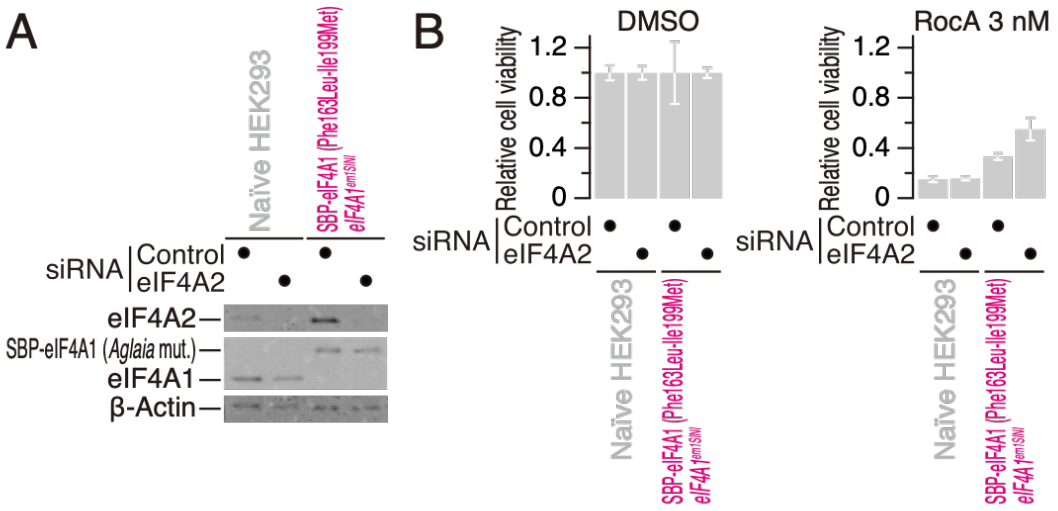

Figure 2.1.1.3. Cell viability assay under the treatment of RocA. A) Western blot of naïve HEK293 cells or eIF4A-eliminated cells; B) Cell viability assay under the treatment of RocA 3 nM or DMSO, the DMSO treated cell viability is normalized to 1.0.

Considering the complicated procedures and possible loss of targets in traditional purification, it would be helpful to establish a method to visualize the proximal proteins that RocA potentially labeled. To achieve that, a bifunctional subunit *O*-nitrobenzoxadiazole (*O*-NBD) attracts our attention due to its "Turn-On" characteristics by providing fluorescence to the proteins around *O*-NBD. The "Turn-On" labeling of *O*-NBD is accomplished by being converted to the fluorescent *N*-NBD after *O*-NBD is conjugated with lysine of proximal proteins (*83*) **(Figure 2.1.1.4)**. Thus, based on the characteristics of *O*-NBD, if we could link *O*-NBD to RocA, we ideally could reach three types of proteins for identifying RocA's targets: 1) the known targets of RocA as eIF4A1 and eIF4A2; 2) eIF4A's interacting factors once they are close enough to eIF4A; 3) alternative targets of RocA instead of eIF4A **(Figure 2.1.1.5)**.

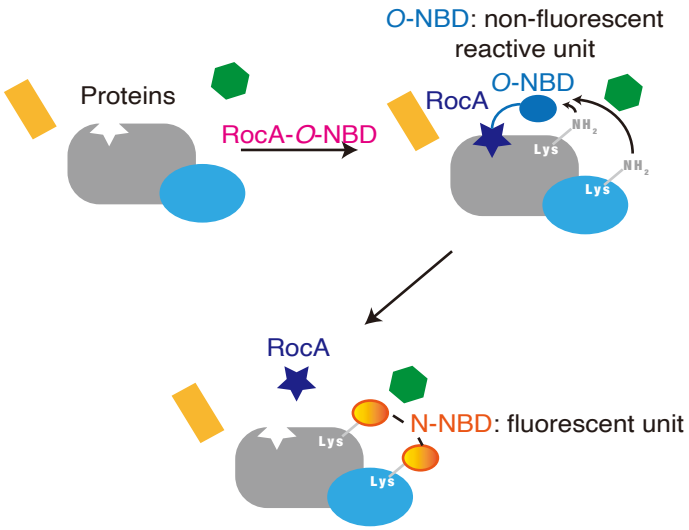

Figure 2.1.1.4. The strategy of proximal labeling by *O*-NBD. The non-fluorescent reactive unit *O*-NBD is highlighted as light blue, while its fluorescent form is labeled as orange; RocA is labeled as dark blue.

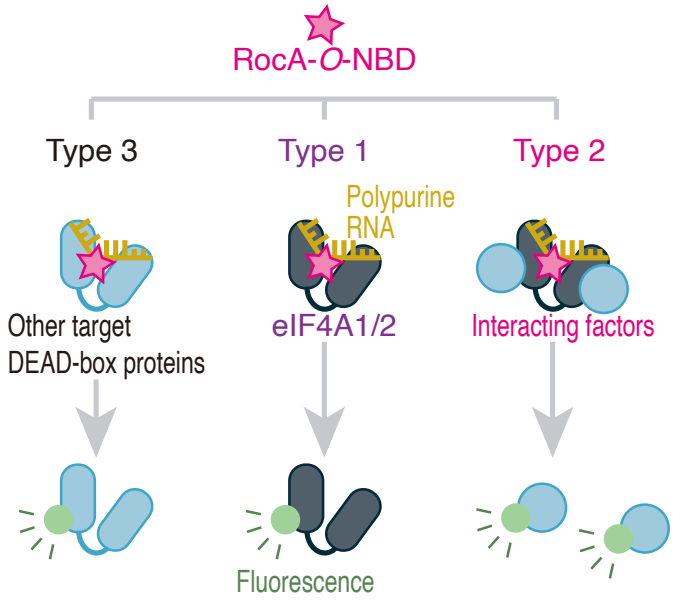

Figure 2.1.1.5. Three types of proximal labeling by RocA-O-NBD.

Here, I collaborated with Koichi Fujiwara, Mikiko Sodeoka, and Kosuke Dodo, who successfully synthesized an *O*-NBD linked RocA, RocA-*O*-NBD, through a di-methylamide

group that could contact neither eIF4A nor polypurine RNA **(Figure 2.1.1.6)**. Before applying it to exploring new targets, I validated its functional activity by applying it to the rabbit reticulocyte lysates (RRL) translation system. To sensitize the translational reaction in RRL, I used a polypurine-harbored reporter to sensitize RocA-induced translation repression in consideration of RocA's polypurine sequence preference (*73*). Consequently, RocA-*O*-NBD presents intense translation repression onto this reporter similarly to RocA, indicating RocA-*O*-NBD kept the primary attributes of RocA as a translational inhibitor **(Figure 2.1.1.7 right)**. As a control, CAA-containing reporter only shows limited translation repression under treatment with RocA-*O*-NBD or RocA **(Figure 2.1.1.7 left)**. Except for the assessment of translation repression, Mari Mito and Shintaro Iwasaki also supportively validated the targeting of eIF4A by RocA-*O*-NBD through immunoprecipitation of *O*-NBD from RRL and subsequent Western blotting **(Figure 2.1.1.8)**. Taken together, RocA-*O*-NBD kept the properties of RocA, including translation repression and targeting, which makes it a plausible tool to investigate the possible targets of RocA.

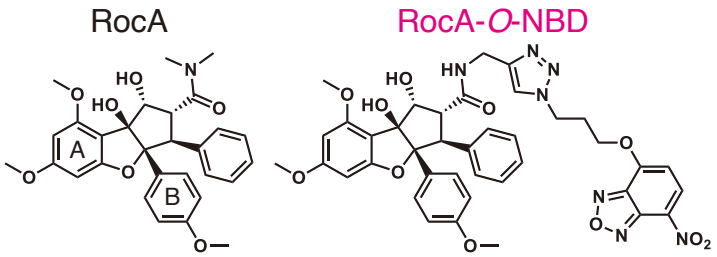

Figure 2.1.1.6. Chemical structure of RocA and RocA-*O*-NBD. RocA-*O*-NBD, highlighted as magenta, is synthesized by conjugating *O*-NBD to RocA by a di-methylamide group and conducted by Koichi Fujiwara and Kosuke Dodo.

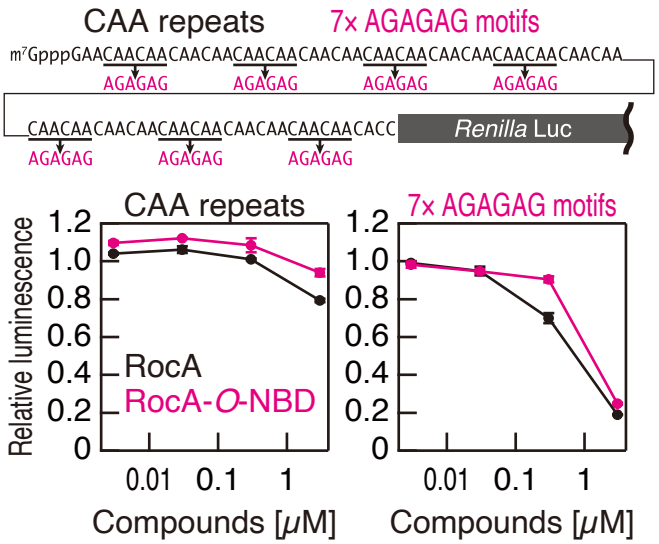

Figure 2.1.1.7. Translation repression by RocA or RocA-*O*-NBD on polypurine (7X AGAGAG motifs) or CAA repeats containing reporters. The arrow in the schematic points to the location of AGAGAG repeats or CAA repeats, and 7 x AGAGAG reporter is highlighted as magenta.

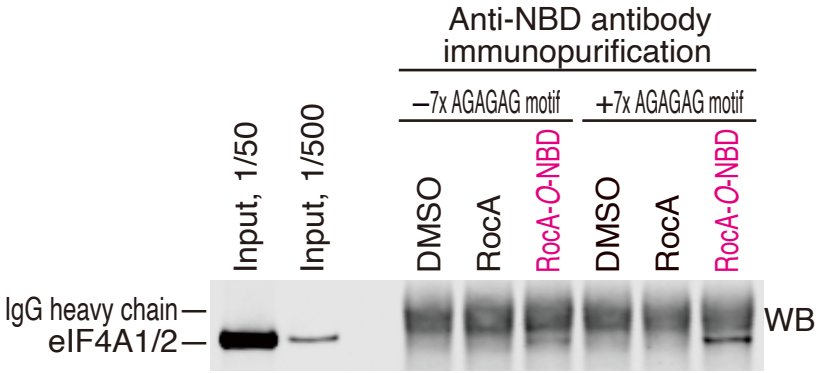

Figure 2.1.1.8. eIF4A1/2 detection by western blot after anti-NBD immunopurification. 7 x AGAGAG motif is added to enhance the binding efficiency. The input is diluted 50 or 500 times for checking the size eIF4A1/eIF4A2, and RocA-*O*-NBD is highlighted as magenta. Conducted by Mari Mito and Shintaro Iwasaki.

Next, I sought to evaluate RocA-*O*-NBD's visibility and labeling specificity in a more purified system. Using recombinant human eIF4A1 and short polypurine RNAs (FAM-labeled $[AG]_{10}$) as materials, RocA-*O*-NBD presented excellent visibility by specifically and

fluorescently labeling eIF4A1 only in the presence of polypurine RNAs **(Figure 2.1.1.9)**, consistent with a previous report that RocA targets eIF4A by enhancing the affinity between eIF4A and polypurine sequences (*73*). Besides that, mutated eIF4A1 with RocA-resistant residues (Phe163Leu-IIe199Met) showed strong resistance to RocA-*O*-NBD's labeling **(Figure 2.1.1.9)**.

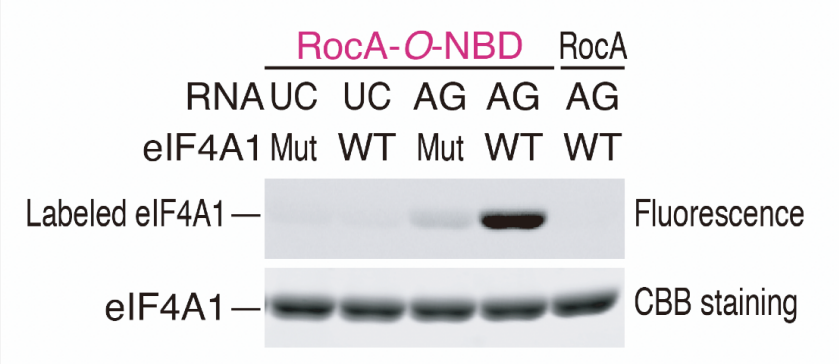

Figure 2.1.1.9. RocA-*O*-NBD labeling of recombinant proteins. The WT means the human eIF4A1 WT proteins, and Mut means the human eIF4A1 proteins but with RocA-resistant residues Phe163Leu-Ile199Met. AG or UC means the FAM-labeled $[AG]_{10}$ or FAM-labeled $[UC]_{10}$ RNAs.

Given that *O*-NBD can only react with lysine in a limited distance (*83*), and to make sure RocA-*O*-NBD labels eIF4A at a suitable position. After applying RocA-*O*-NBD into RRL lysates, Miwako Asanuma did liquid chromatography-mass spectrometry with a laser-induced fluorescence detector (LC-fluorescence-MS) (*83*) to identify the fluorescence-tagged peptide in rabbit eIF4A1 **(Figure 2.1.1.10-A, B, C)**, the precisely annotated residue at Lys166 of rabbit eIF4A1 told us RocA-*O*-NBD labeled Lys166 of eIF4A1 in a proximally proper position as revealed from the structure **(Figure 2.1.1.11)**. Also, considering the high conservation between rabbit eIF4A1 and human eIF4A1, I concluded RocA-*O*-NBD would also similarly tag human eIF4A1. For eIF4A2, LC-fluorescence-MS also confirmed that RocA-*O*-NBD fluorescently

tagged eIF4A2 in the essentially same position as eIF4A1 **(Figure 2.1.1.10-D, E, F)**, furtherly proving RocA-*O*-NBD/RocA targets both eIF4A1 and eIF4A2. Overall, RocA-*O*-NBD can be an effective tool to detect RocA's targets.

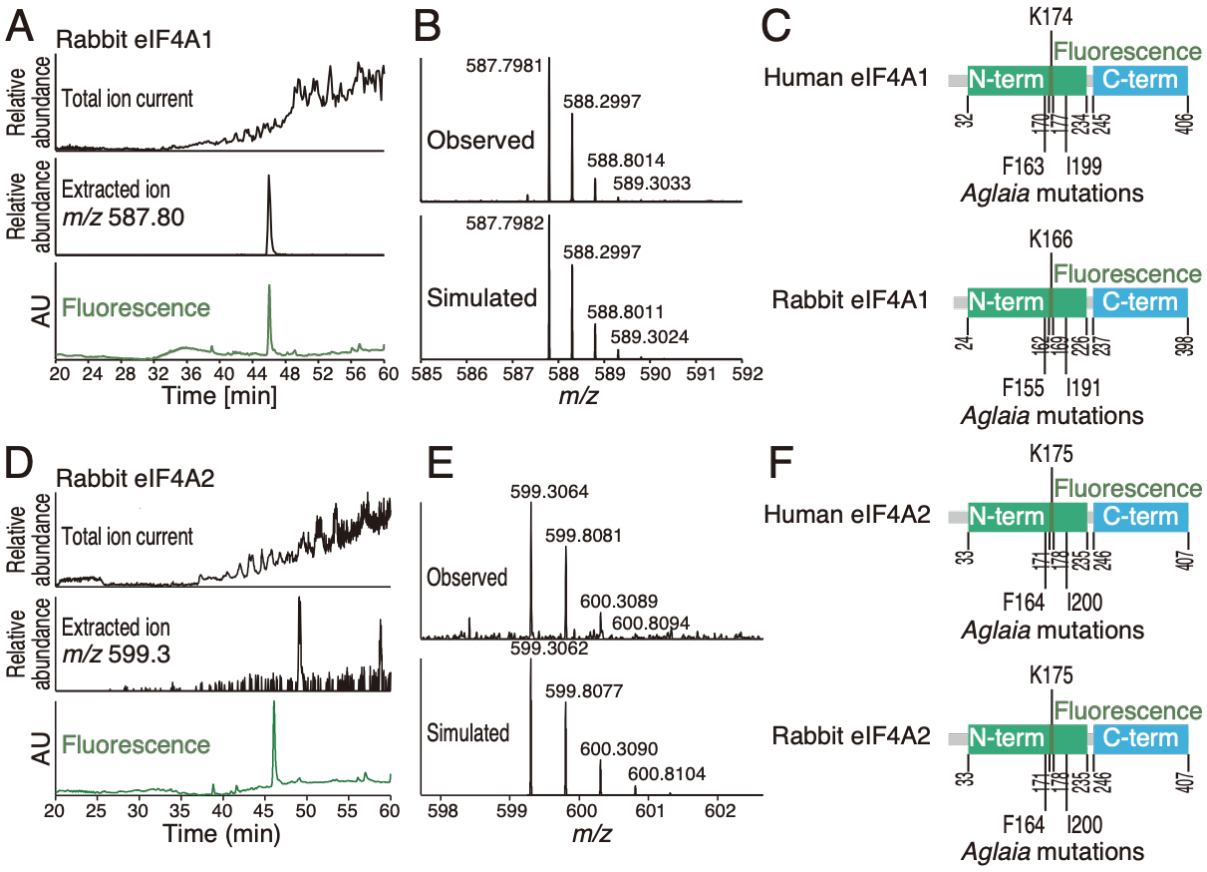

Figure 2.1.1.10. Liquid chromatography-mass spectrometry with a laser-induced fluorescence detector (LC-fluorescence-MS) detection of RocA-*O*-NBD labeling. (A) Chromatograms for the total ion current (top), extracted ions in the range of m/z 587.79–587.80 corresponding to N-NBD-[Tyr162–Lys169] of rabbit eIF4A1 (middle), and laser-induced fluorescence (LIF) (bottom). (B) Observed (top) and simulated (bottom) mass spectrum of the *N*-NBD-[Tyr162–Lys169] of rabbit eIF4A1. (C) Schematic of lysine labeling by RocA-*O*-NBD in human and rabbit eIF4A1. (D) Chromatograms for the total ion current (top), extracted ions in the range of m/z 599.30–599.31 corresponding to the *N*-NBD-[Tyr171–Lys178] of rabbit eIF4A2 (middle), and LIF (bottom). (E) Observed (top) and simulated (bottom) mass spectrum of the *N*-NBD-[Tyr171–

Lys178] of rabbit eIF4A2. (F) Schematic of lysine labeling by RocA-*O*-NBD in human and rabbit eIF4A2. Conducted by Miwako Asanuma.

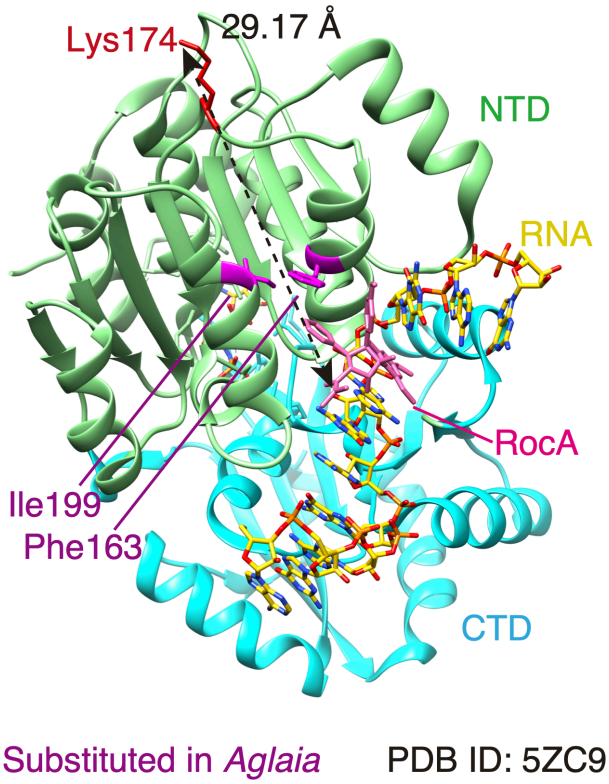

Figure 2.1.1.11. Structure of human eIF4A1·RocA·RNA. The labeling site of RocA-*O*-NBD, Lys174, is highlighted in red.

2.1.2. RocA alternatively targets DDX3X

As an application of RocA-*O*-NBD into discovering new targets/target of RocA, Mari Mito and Shintaro Iwasaki added RocA-*O*-NBD into rabbit reticulocyte lysates and did electrophoresis. After exposing the gel to fluorescence, several proteins were conferred to fluorescence by RocA-*O*-NBD. This labeling could be enhanced by adding 7 x AGAGAG

motif reporter mRNAs. To further identify what kind of proteins are tagged by RocA-*O*-NBD, subsequent mass spectrometry was performed, eIF3A, eIF4G1, eIF4B, DDX3X eIF4E, eIF4H, as well as eIF4A1/2 were identified as RocA-*O*-NBD labeled proteins **(Figure 2.1.2.1-right)**. Among them, eIF4A1/2 were regarded as known targets of Type I **(Figure 2.1.2.1-left)**, but for eIF3A, eIF4G1, eIF4B, eIF4E, and eIF4H, they are known to interact with eIF4A1/2 by forming complexes with eIF4F or PIC (pre-initiation complex) (*24*). Hence, they are classified into Type II **(Figure 2.1.2.1-left),** considering RocA-O-NBD possibly labels them because of their interaction with eIF4A1/2. Except for all the above proteins, I was convinced that DDX3X is probably the only protein that RocA directly targeted to as Type III showed **(Figure 2.1.2.1-left)**. Also, given that eIF4A1, eIF4A2, and DDX3X are from the same DEAD-box family, which shares a similar conserved structure, I hypothesized that RocA might affect DDX3X with eIF4A coordinately and similarly. In addition, to briefly address RocA's targeting to DDX3X, I prepared recombinant DDX3X proteins with the catalytic core (amino acids 132-607) (*84*) and checked RocA-*O*-NBD's labeling to the protein, similar to eIF4A, RocA-*O*-NBD could label DDX3X when FAM-labeled polypurine RNA ($[AG]_{10}$) were added **(Figure 2.1.2.2)**.

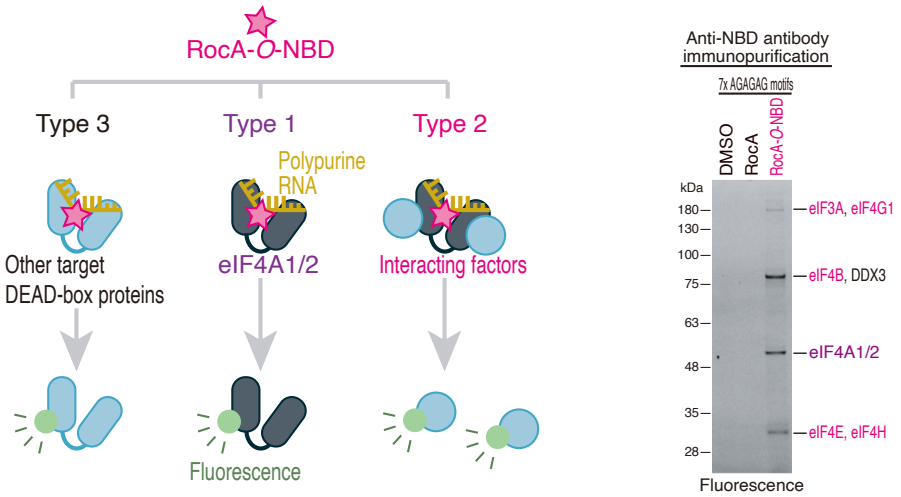

Figure 2.1.2.1. Mass spectrometry identification of potential proteins labeled by RocA-*O*-NBD. Left) RocA-O-NBD can label types of proteins; Right) The proteins identified by mass spectrometry. Conducted by Mari Mito, Miwako Asanuma, and Shintaro Iwasaki.

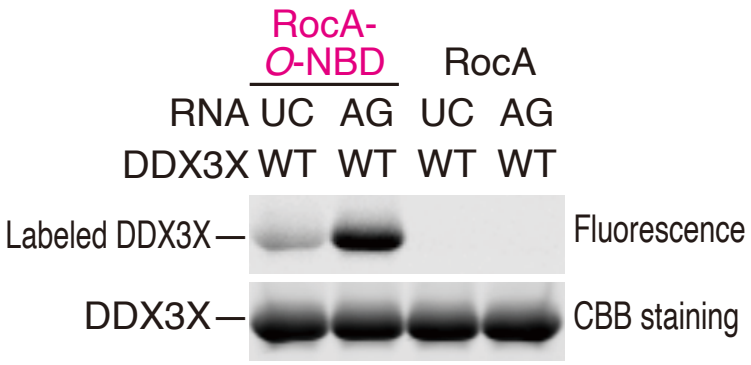

Figure 2.1.2.2. Labeling of recombinant DDX3X proteins by RocA-*O*-NBD (or RocA) in the presence of polypurine (AG) or polypyrimidine (UC), in which AG represents a FAM-labeled $[AG]_{10}$ RNA, and UC represents a FAM-labeled $[UC]_{10}$ RNA.

Mass spectrometry analysis performed by Miwako Asanuma furtherly validated RocA-*O*-NBD could provide fluorescence to DDX3X in the same loop as eIF4A1 **(Figure 2.1.2.3)**, again indicating the direct targeting of DDX3X by RocA. Consistent with this, I also verified RocA's targeting to DDX3 *in cellulo* by knocking down DDX3 and eIF4A2 in HEK293 SBP-eIF4A1 (Phe163Leu-Ile199Met) *eIF4A1*^{em1SINI}. A gradual cell rescue following RocA-resistant eIF4A1 (HEK293 SBP-eIF4A1 (Phe163Leu-Ile199Met) *eIF4A1*^{em1SINI}), RocA-resistant eIF4A1 + reducing eIF4A2, and RocA-resistant eIF4A1 + reducing eIF4A2 + reducing DDX3, indicated RocA inhibited cell growth by targeting DDX3 and eIF4A1/2 *in cellulo* **(Figure 2.1.2.4)**. Taking together, DDX3 was identified as a new target of RocA besides its known

targets eIF4A1 and eIF4A2, and its targeting was confirmed from both intracellular and extracellular levels.

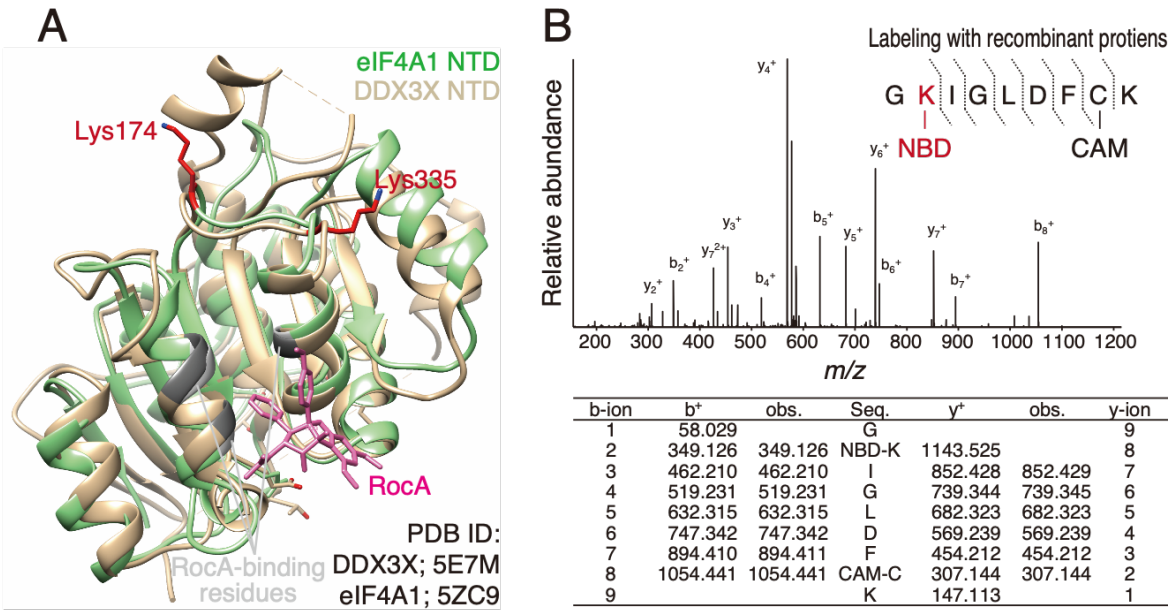

b-ion	b+	obs.	Seq.	y+	obs.	y-ion
1	58.029		G			9
2	349.126	349.126	NBD-K	1143.525		8
3	462.210	462.210	I	852.428	852.429	7
4	519.231	519.231	G	739.344	739.345	6
5	632.315	632.315	L	682.323	682.323	5
6	747.342	747.342	D	569.239	569.239	4
7	894.410	894.411	F	454.212	454.212	3
8	1054.441	1054.441	CAM-C	307.144	307.144	2
9			K	147.113		1

Figure 2.1.2.3. Structural comparison (A) and LC-fluorescence-MS/MS (B) reveal the labeling location of RocA-*O*-NBD (highlighted as red color) in DDX3 and eIF4A1.

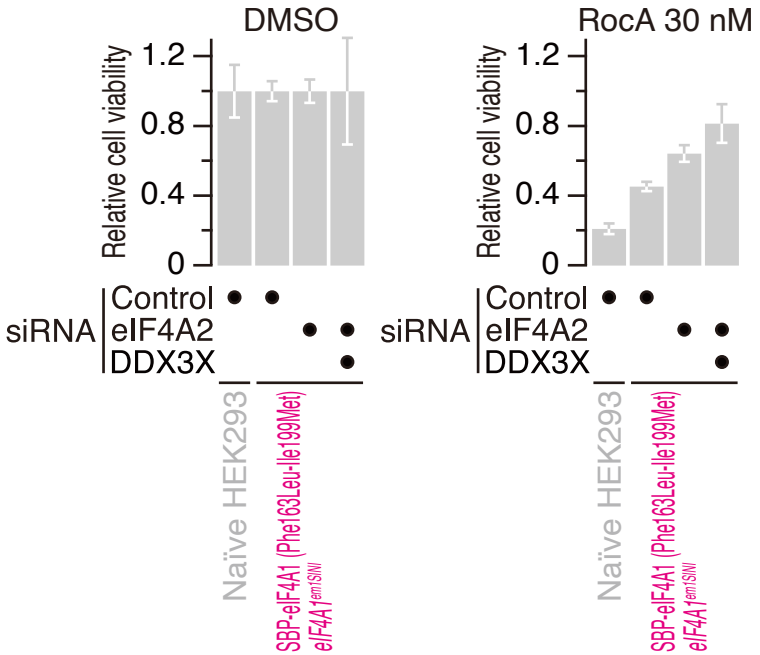

Figure 2.1.2.4. Cell viability assay under the treatment of RocA or DMSO. Left) Cell viability under the treatment of DMSO, which is normalized to 1.0; Right) Cell viability under the treatment of RocA 30 nM. Yuichi Shichino and Shintaro Iwasaki conducted the preliminary experiment.

2.2. Mechanisms of RocA

2.2.1. RocA confers DDX3 to polypurine binding ATP-independently

Since RocA was known to convert eIF4A into a polypurine preferred protein in an ATP-independent manner (*73*), I first sought to investigate the sequence preference of its newly identified target, DDX3. Together with the result that RocA-*O*-NBD conferred intense labeling to recombinant DDX3X when polypurine RNAs were added, I did the fluorescence polarization (FP) assay **(Figure 2.2.1.1)** to test DDX3's binding preference between FAM-labeled polypurine ($[AG]_{10}$) and FAM-labeled polypyrimidine ($[UC]_{10}$) RNAs with or without RocA. Like eIF4A1/2's polypurine preference **(Also see Figure 2.1.1.1)**, DDX3X also presented a strong preference for polypurine RNAs under the treatment of RocA **(Figure 2.2.1.2)** even without ATP, which means RocA inhibits eIF4A or DDX3 by clamping either of them onto polypurine sequences ATP-independently.

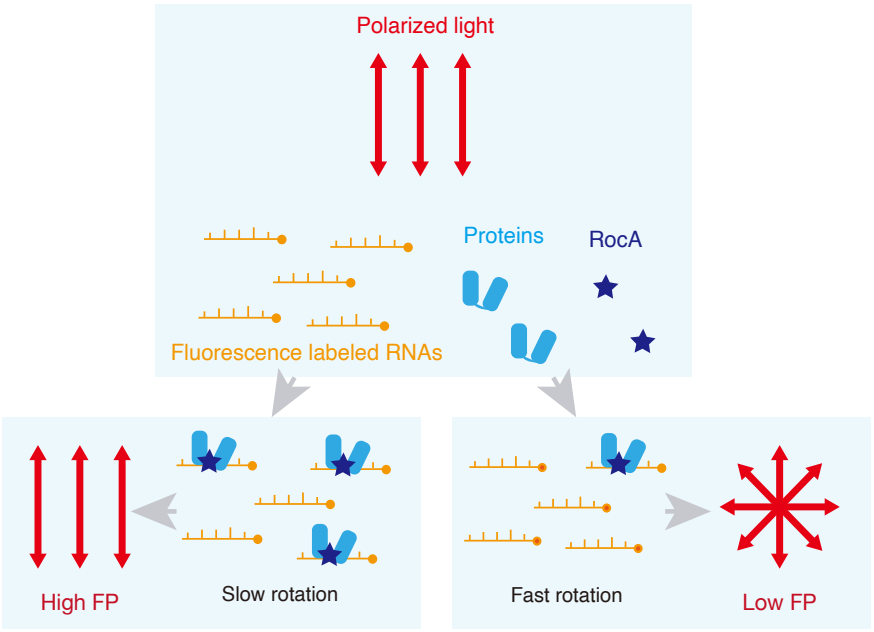

Figure 2.2.1.1. The principle of fluorescence polarization assay. Strong binding between RNAs and proteins leads to the high maintenance of polarization of light (Left down); Weak binding leads to low fluorescence polarization of light (Right down).

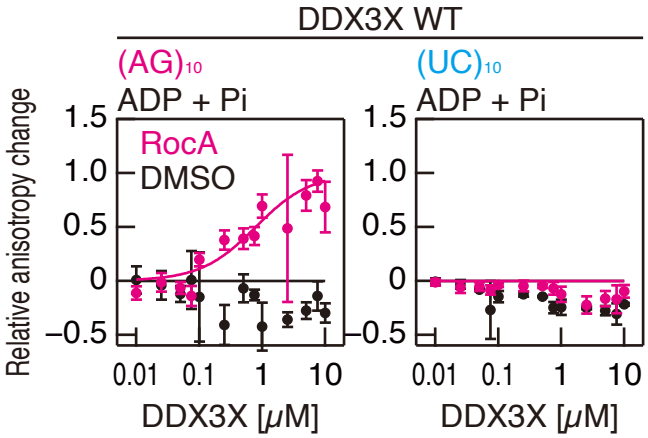

Figure 2.2.1.2. Fluorescence polarization test for DDX3X and polypurine ($(AG)_{10}$) or polypyrimidine ($(UC)_{10}$) RNAs in the presence of ADP + Pi.

However, because the sequence combinations applied into the FP assay were very limited (polypurine and polypyrimidine), I next aimed to explore the sequence preference of RocA

bounded DDX3 more deeply. To do that, I took full advantage of a well-established method, Bind-n-Seq (*85*), in which randomized RNA motifs were mixed with affinity-tagged recombinant proteins (In this study SBP-eIF4A1 and SBP-DDX3X, **Figure 2.2.1.3-A**).

Following adding RocA, the proteins were pulled down for downstream RNA extraction. Consequently, deep sequencing of the extracted RNAs could give us an overlook of the preferred motifs for the recombinant proteins **(Figure 2.2.1.3-B)**. After Bind-n-Seq, the reads' quality was first checked according to the length (30 nt) of the enriched RNA **(Figure 2.2.1.4)**. Then, I calculated the motifs retained onto DDX3 with RocA but without ATP. As a result, I found that DDX3 presented a strong polypurine preference **(Figure 2.2.1.5-A)**. Similarly, I also validated eIF4A1's sequence preference of polypurine as reported before (*73*) **(Figure 2.2.1.5-B)**. By correlating the enriched motifs of both proteins, I noticed that polypurine motifs were obviously popped out, indicating a parallel sequence preference between DDX3 and eIF4A **(Figure 2.2.1.5-C)**. Moreover, I also checked DDX3's sequence preference in the presence of ATP (Non-hydrolyzed form AMP-PNP used). After normalizing the RocA-treated group to the control of the DMSO-treated group, I observed that RocA maintained DDX3's preference for polypurine motifs even in the presence of ATP **(Figure 2.2.1.6)**. Thus, I concluded that RocA targeted DDX3 and clamped DDX3 onto polypurine RNAs.

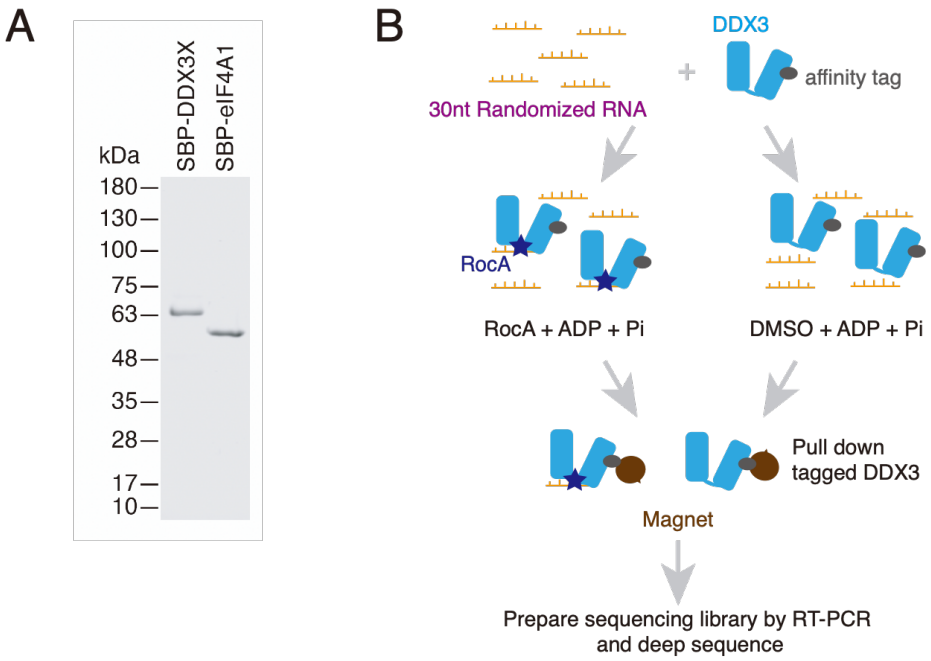

Figure 2.2.1.3. Workflow of Bind-n-Seq. A) Coomassie blue staining of proteins with affinity tag. B) Schematic of Bind-n-Seq procedures.

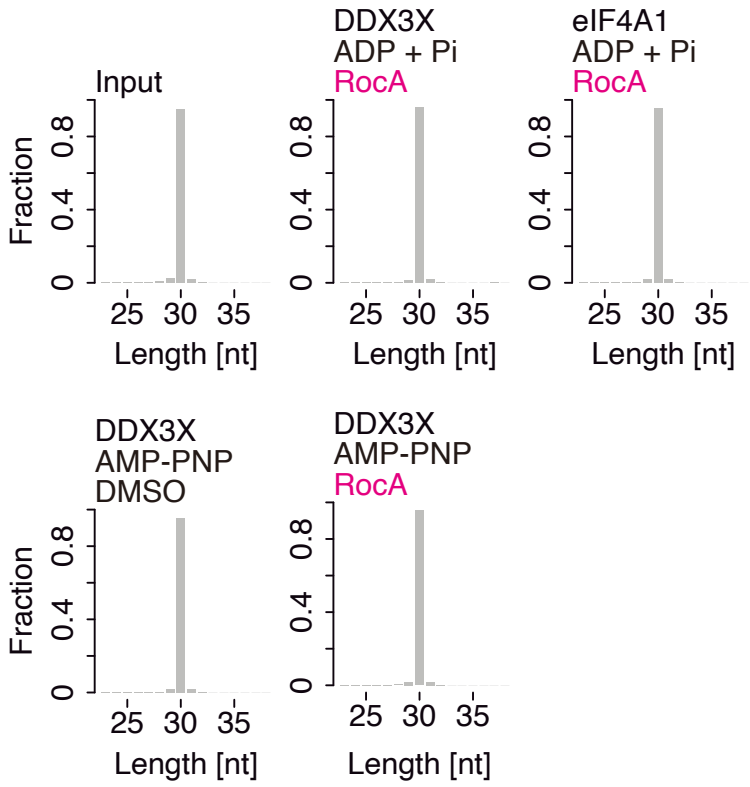

Figure 2.2.1.4. Quality check of Bind-n-Seq. Fraction means the fraction of enriched reads from Bind-n-Seq; Length means the length of enriched motifs.

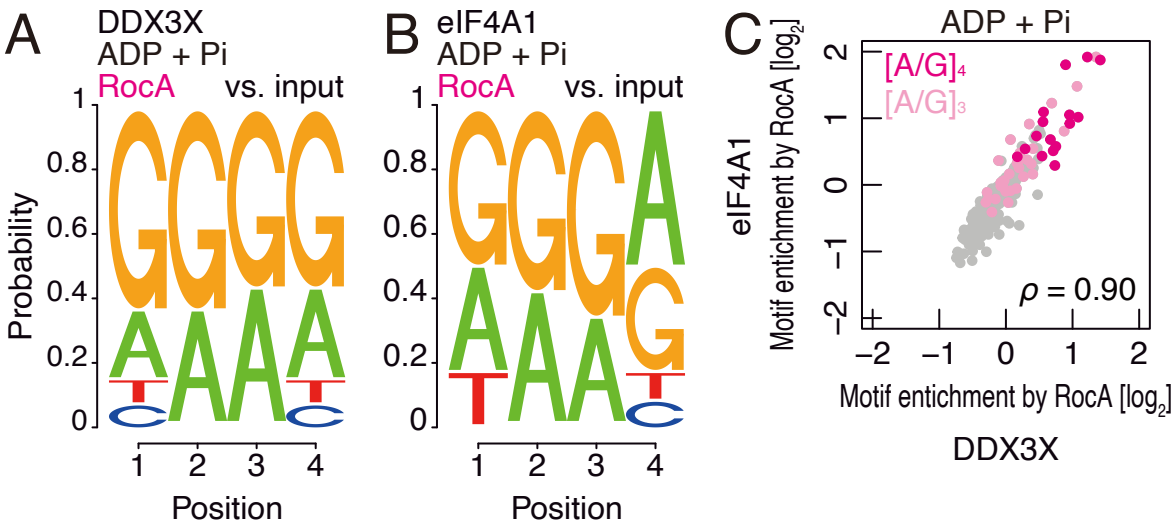

Figure 2.2.1.5. Motifs enriched on A) DDX3X and B) eIF4A1 in the presence of ADP + Pi identified by Bind-n-Seq; C) Correlation of motifs enriched from DDX3 and eIF4A1.

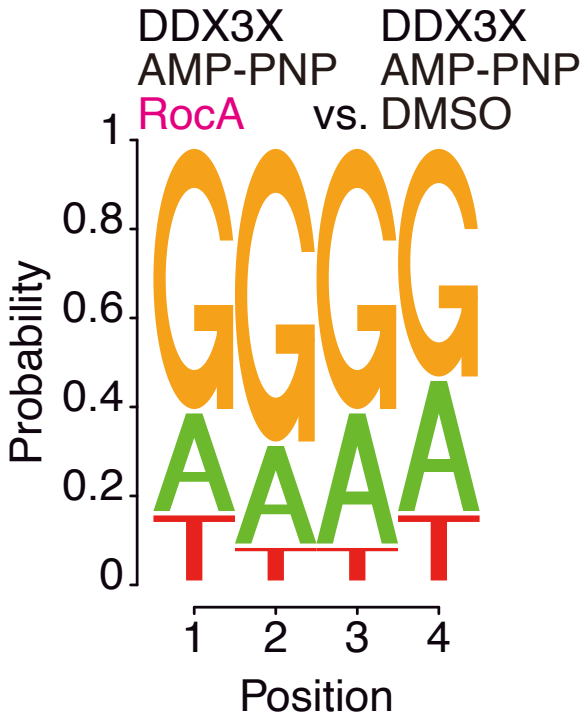

Figure 2.2.1.6. Motifs enriched on DDX3X in the presence of AMP-PNP and RocA after normalizing to DMSO-treated group.

2.2.2. RocA • DDX3 represses translation dominant-negatively

Because RocA enhances eIF4A's affinity with RNAs, the supplement of eIF4A does not simply rescue RocA-induced translation repression but causes a strengthened inhibition (*73*). To investigated if DDX3 is influenced similarly, I supplemented recombinant DDX3X or eIF4A1 proteins into the RRL translation system. After adding polypurine reporters to sensitize the reaction, I saw a significantly repressed translation of about 15% under the treatment of RocA. However, with more eIF4A/DDX3 recombinant proteins supplemented, more translation repression was induced, showing a dominant-negative effect **(Figure 2.2.2.1-A)**. As a control with CAA-reporter, there was no evident translation repression **(Figure 2.2.2.1-B)**, again suggesting DDX3/eIF4A's polypurine preference. Therefore, I concluded that RocA·DDX3 inhibited translation similarly to eIF4A in a dominant-negative way.

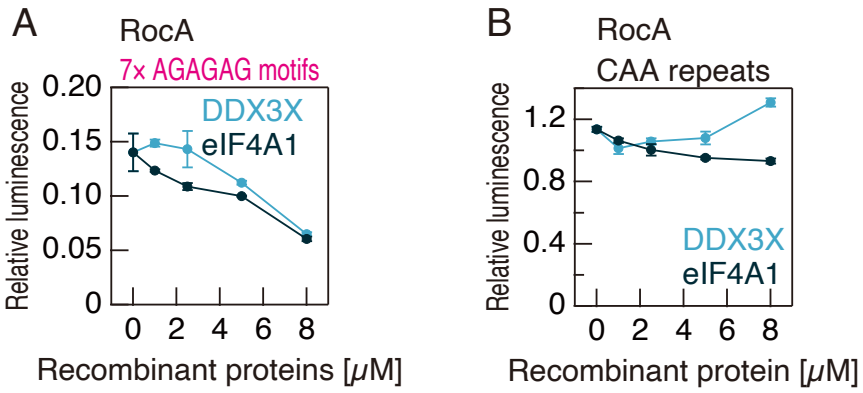

Figure 2.2.2.1. *In vitro* translation test by supplementing recombinant eIF4A1 (black) or DDX3 (light blue) into rabbit reticulocyte lysates system with 1 μM RocA. The relative translation (relative luminescence) is calculated when A) polypurine reporters or B) CAA-containing reporters are added.

Compared to eIF4A1, the dominant-negative translation repression by DDX3X was relatively weaker. This phenomenon can be explained by the relatively weak binding between DDX3·RNA complexes and RocA measured by microscale thermophoresis (Done by Mari Takahashi and Takuhiro Ito) **(Table 1)** or vulnerable DDX3-clamping by RocA calculated from FP assay **(Table 2).** Taken together, I summarized that RocA inhibits translation irrespective of eIF4A/DDX3 binding partners, and more abundant RocA targets would induce more RocA-induced translation repression.

Table 1. Summary of the K_d between the protein·RNA complexes and RocA measured by microscale thermophoresis. (ND means not determined). Conducted by Mari Takahashi and Takuhiro Ito.

	$(AG)_5A$
	AMP-PNP
Protein	RocA
eIF4A1	0.014 ± 0.0023
DDX3X	0.42 ± 0.31
Gln360Pro	3.4 ± 1.5
Gln360leu	ND

Table 2. Summary of the K_d between eIF4A1/2, DDX3, and FAM-labeled RNAs calculated from fluorescence polarization. (ND means not determined).

	$(AG)_{10}$			
	ADP + Pi		AMP-PNP	
Protein	DMSO	RocA	DMSO	RocA
eIF4A1	ND	0.25 ± 0.0092	1.4 ± 0.38	0.15 ± 0.0051
eIF4A2	ND	1.3 ± 0.14	27 ± 8.4	0.14 ± 0.038
DDX3X	ND	0.79 ± 0.14	4.3 ± 0.40	0.17 ± 0.018
Pro324Thr	ND	0.40 ± 0.0079		
Val328Leu	ND	0.20 ± 0.0090		
Gln360Pro	ND	ND	3.3 ± 0.37	
Gln360Leu	ND	ND	1.7 ± 0.066	
Arg363Asn	ND	0.39 ± 0.0087		

2.2.3. The abundance of eIF4A/DDX3 suggests RocA's sensitivity

As described above, cancer cells sense RocA from a vast magnitude for unknown reasons (*57*). The clarified dominant-negative mechanisms of RocA in the RRL translation system drove me to hypothetically link the abundance of eIF4A/DDX3 to RocA sensitivity, and I assumed the distinctive eIF4A/DDX3 abundance in different cancer cells leads to distinctive translation repression and distinctive cell death as a result **(Figure 2.2.3.1)**. To validate this hypothesis, I decided to choose cancer cells with different amounts of eIF4A/DDX3 proteins. Given the considerable number of cancer cells, I focused on two RNA-Seq databases (*86, 87*) to look for the candidate cancer cells harboring significant eIF4A/DDX3. By correlating RNA abundance of eIF4A and DDX3, I picked out four of them from highly correlated ones **(Figure 2.2.3.2).** To verify these four cancer cells also have different protein abundance, I did Western blot to visualize their protein abundance. As a validation, I saw a significantly increased protein abundance from Hs 936.T, A375, and NCI-H1650 to NCI-H520 **(Figure 2.2.3.3)**. To test their sensitivity to RocA, the half-maximal inhibitory concentration (IC_{50}) of RocA was calculated as a result of treating cancer cells with a gradient concentration of RocA **(Figure 2.2.3.4)**. Corresponding to the dominant-negative assumption, I observed an opposite trend of RocA sensitivity with their eIF4A/DDX3 abundance, suggesting a negative correlation between RocA sensitivity and eIF4A/DDX3 abundance **(Figure 2.2.3.5)**.

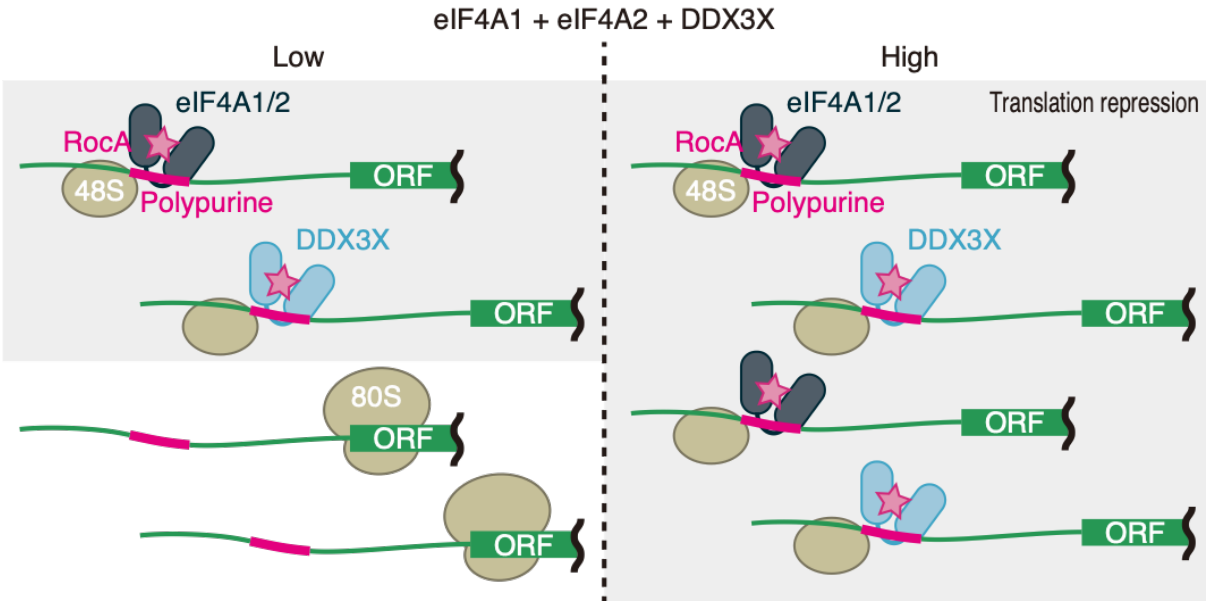

Figure 2.2.3.1. The model of dominant-negative effects of RocA in cancer cells. Low means cancer cells with a low abundance of eIF4A1/2 and DDX3, and high means the cells with a higher abundance of eIF4A1/2 and DDX3.

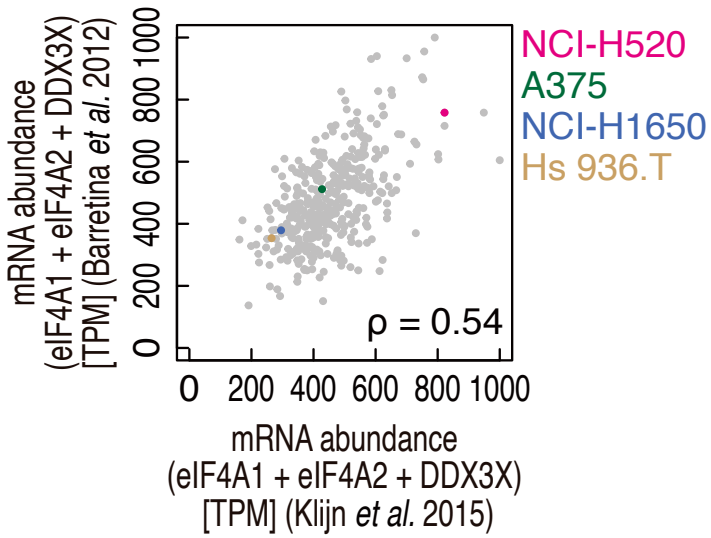

Figure 2.2.3.2. Correlated RNA abundance of eIF4A1+eIF4A2+DDX3X from two RNA-Seq databases (*86, 87*), in which colors highlight the four selected cancer cells.

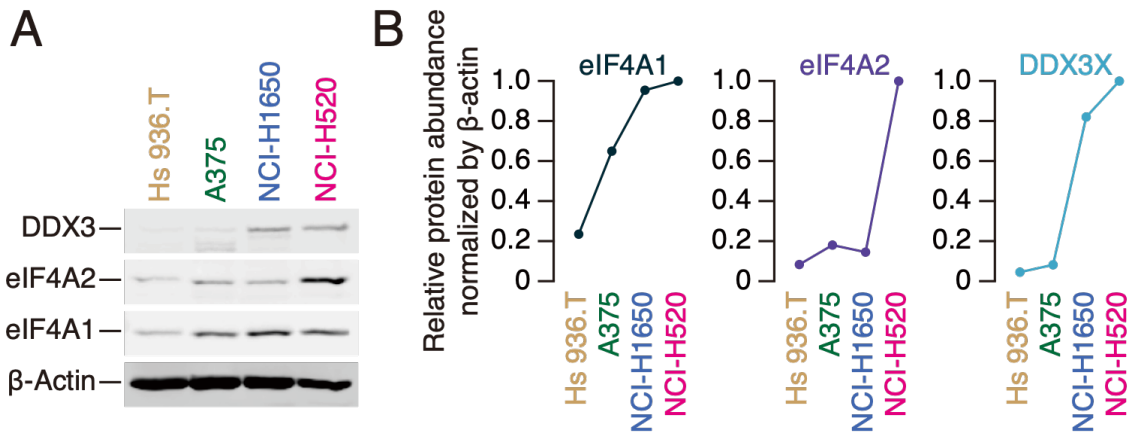

Figure 2.2.3.3. Protein abundance of four cancer cells used in this study. A) Western blot of DDX3, eIF4A1/2, and β-actin of Hs 936.T, A375, NCI-H1650, and NCI-H520; B) Quantification of protein abundance of eIF4A1/2 and DDX3 from A).

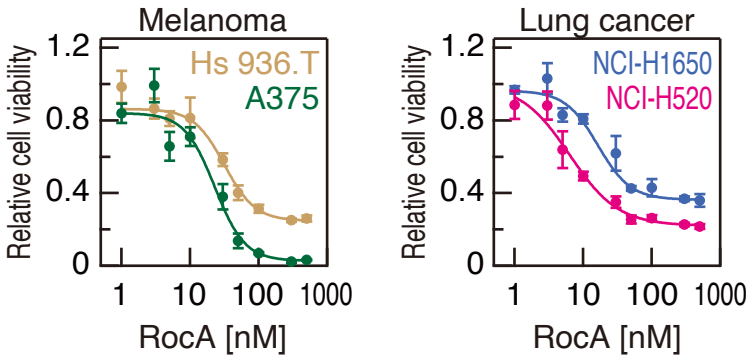

Figure 2.2.3.4. Cell viability test for Hs 936.T, A375, NCI-H1650, and NCI-H520. Left) Comparison of cell response to increased RocA for melanoma, Hs 936.T and A375; Right) Comparison of cell response to increased RocA for lung cancer cells, NCI-H1650 and NCI-H520.

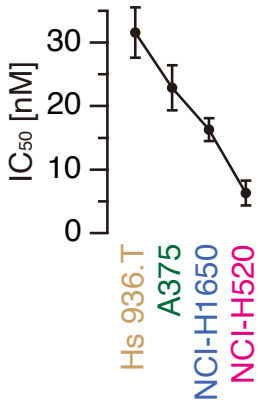

Figure 2.2.3.5. Correlation between RocA IC_{50} and eIF4A+DDX3 protein abundance.

Given the tight relationship between translation repression and cell death, I next sought to investigate if there is also a negative correlation between eIF4A/DDX3 abundance and RocA-induced translation repression in cells. To check the translational change on a more sensitive level, I used ribosome profiling in order to give a profound snapshot of the global translational change **(Figure 2.2.3.6)**. Ribosome profiling (Ribo-Seq) can provide direct insight into the ribosome-protected RNA fragments by digesting RNA areas not covered by ribosomes. In Ribo-Seq, distinctive samples were distinguished by ligating different linkers. The library could be built for deep sequencing following ribosomal RNAs' depletion, reverse transcription, and PCR amplification. As a result, Ribo-Seq led us to directly understand the translational level in different conditions (*88-91*).

Applying Ribo-Seq to RocA-treated cancer cells, I did observe the most prominent translation repression for NCI-H520, which harbors the most abundant RocA targets **(Figure 2.2.3.3-A).** Although the higher concentration of RocA 3 μM saturated the translation repression and made the gradient of translation not so visible **(Figure 2.2.3.7-B)**, the treatment of RocA 0.3 μM clearly showed that the cancer cells with more abundant eIF4A/DDX3 were more responsive to RocA **(Figure 2.2.3.7-A)**, suggesting the RocA-induced translation repression is highly related to the protein level of eIF4A/DDX3. Moreover, in each cell type, the transcripts with

polypurine motifs in their 5' UTR were more repressed by RocA **(Figure 2.2.3.7)**, verifying the polypurine preference of RocA.

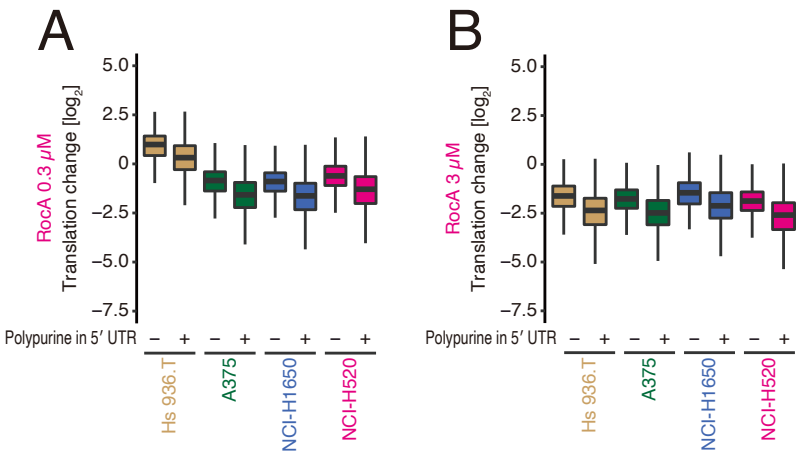

Figure 2.2.3.7. The translational change led by A) 0.3 μM or B) 3 μM RocA. The "+" or "-" means there are or there are not polypurine motifs in the 5' UTR.

Overall, the abundance of RocA targets in cancer cells is tightly related to their differential RocA sensitivity. Coupled with the dominant-negative translation repression, RocA probably inhibits translation differently and then induced different magnitudes of cancer cell death. Above all, the abundance of RocA targets in cancer cells can suggest their sensitivity to RocA, thus promisingly providing clinical guidance for the potential usage of rocaglates.

2.3. Resistance of RocA

2.3.1. *Aglaia* resists RocA toxicity by substituting specific residues

As introduced above, the targets of RocA, eIF4A and DDX3, play essential roles in all eukaryotic species. However, as the origin of RocA, the plant *Aglaia* incredibly escapes from

RocA's toxicity. Previous studies about RocA's resistance focused on its known target eIF4A. From assembled eIF4A transcriptome of *Aglaia*, several unique mutations were identified in the potential binding pocket of RocA (*75*). Mutagenesis of human eIF4A1 by placing *Aglaia* mutations confers strong resistance to RocA, thus indicating *Aglaia* eIF4A evolved with specific mutations to abolish RocA's binding. Furthermore, the resolved eIF4A·RocA·RNA structure highlights the importance of these residues, suggesting these substitutions alters the binding cavity of RocA and abandons RocA's incorporation (*75*).

As a newly identified target of RocA, DDX3, if there is any resistance mode in *Aglaia* DDX3 requires further investigation. Thus, the transcriptome of *Aglaia* DDX3 was assembled and aligned with multiple other species, including human, yeast, and plant **(Figure 2.3.1.1)**. In the potential binding pocket of RocA, several substitutions in DDX3 were found, such as Pro324Thr, Val328Leu, Gln360Pro, Gln360Leu, and Arg363Asn **(Figure 2.3.1.1, highlighted as magenta)**. Then, I inspected the significance of these residues by placing them into human DDX3X individually. In the case of human DDX3X WT, a firm clamping onto polypurine sequences by RocA was observed even in the absence of ATP **(Figure 2.3.1.2)**, underlining the independence of ATP and polypurine preference of RocA. Based on RocA's characteristics and to test the resistance of *Aglaia*-mutated human DDX3 to RocA, I used the ADP, Pi, and polypurine RNAs in FP assay in consideration of the ATP-independency as a hallmark of RocA targeting. The calculation of anisotropy changes for different kinds of recombinant DDX3 **(Figure 2.3.1.3)** told us Gln360Pro or Gln360Leu abolished RocA's clamping **(Figure 2.3.1.4)**, indicating the position Gln360 is critical for *Aglaia* DDX3's resistance to RocA. Because of the structural conservation between eIF4A1 and DDX3, I also aligned the published eIF4·RocA·RNA structure (PDB: 5ZC9) with DDX3X (PDB: 5E7M) and found that Gln360 resides in a very close position with RocA **(Figure 2.3.1.5)**. This proximal distance indicates

Aglaia DDX3 probably resists RocA's toxicity by altering the cavity conformation that RocA potentially targets.

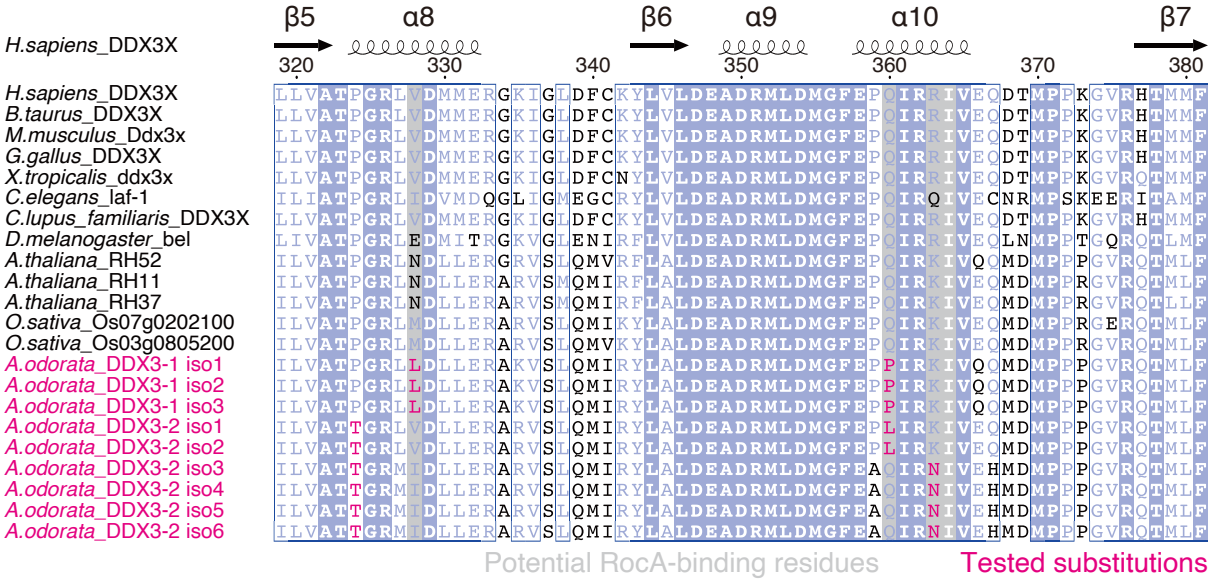

Figure 2.3.1.1. Alignment of assembled *Aglaia* (*A. odorata*) DDX3 transcriptome and multiple other species. The potential binding residues of RocA are highlighted as gray, and tested residues in this study are highlighted as magenta. The assembly was conducted by Shintaro Iwasaki.

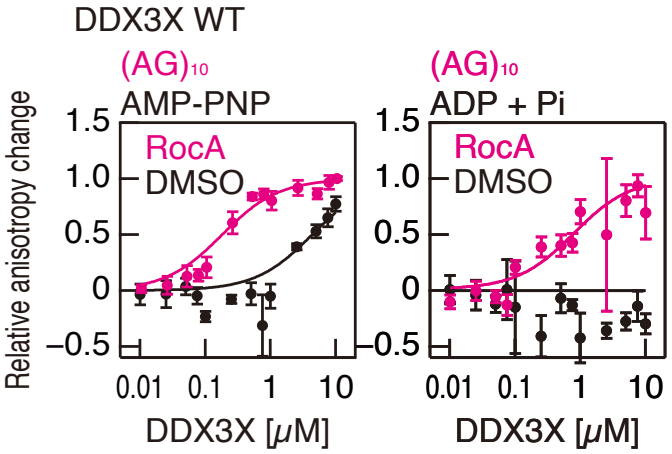

Figure 2.3.1.2. Fluorescence polarization test of human DDX3X WT and polypurine RNAs (FAM-labeled $[AG]_{10}$) in the presence/absence of ATP (non-hydrolyzable analog of ATP: AMP-PNP).

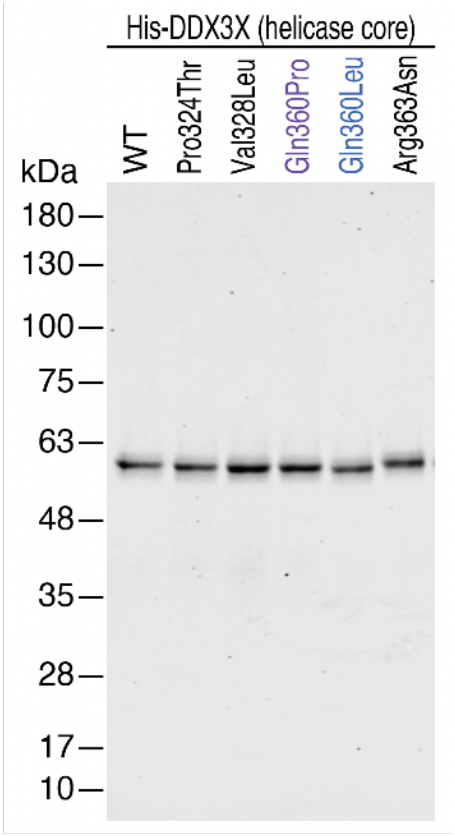

Figure 2.3.1.3. Coomassie blue staining of recombinant DDX3X proteins used in this study.

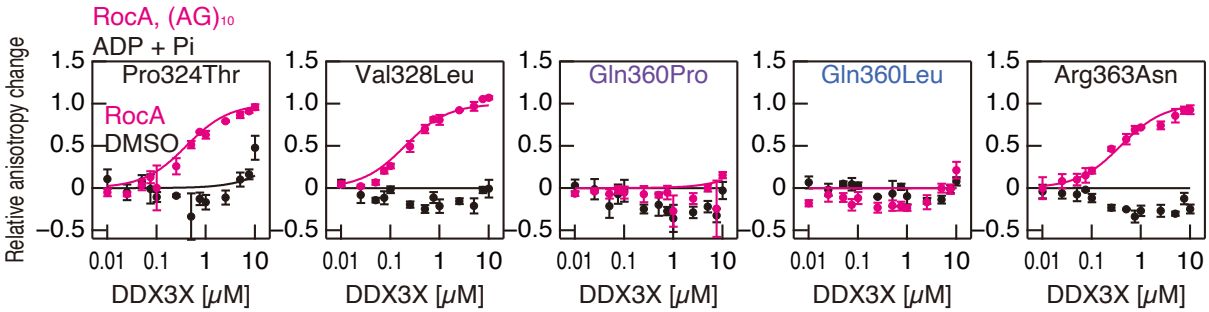

Figure 2.3.1.4. Fluorescence polarization test of mutated human DDX3X and polypurine RNAs (FAM-labeled $[AG]_{10}$) in the absence of ATP (ADP + Pi).

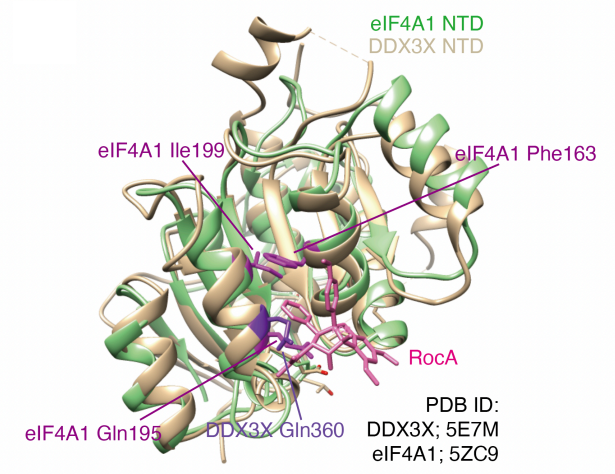

Figure 2.3.1.5. Aligned eIF4A1·RocA·RNA structure (PDB: 5ZC9) with DDX3X structure (5E7M). The mutations identified from the *Aglaia* transcriptome are highlighted as purple in eIF4A1 and magenta in DDX3X.

To exclude the possibility that Gln360 discards DDX3's basic function, I performed FP assay for all of these proteins but with AMP-PNP (Non-hydrolyzable analog of ATP) and DMSO. The result suggested that the mutation Gln360 identified from *Aglaia* DDX3 transcriptome did not induce the loss of basic function **(Figure 2.3.1.6-A)**, indicating that Gln360 only affects RocA's binding to *Aglaia* DDX3. As a validation, I checked RocA-*O*-NBD's labeling efficiency for the recombinant DDX3 Gln360Pro/Leu, and the result confirmed Gln360Pro/Leu presented a strong resistance to RocA-*O*-NBD's tagging **(Figure 2.3.1.6-B).**

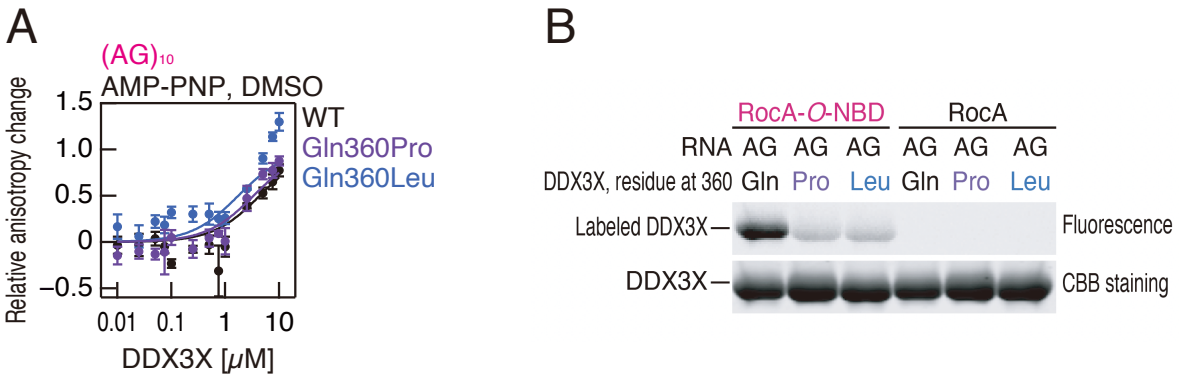

Figure 2.3.1.6. Characterization of *Aglaia* mutated DDX3X. A) The basic binding revealed by fluorescence polarization test between recombinant proteins and RNA in the presence of DMSO and AMP-PNP (ATP analog). B) RocA-*O*-NBD labeling for recombinant DDX3X proteins with polypurine (FAM-labeled $[AG]_{10}$) or polypyrimidine (FAM-labeled $[UC]_{10}$) added.

Above all, the resistance of *Aglaia* to RocA is mainly accomplished by transforming its eIF4A and DDX3 into a RocA-resistant mode. This transformation is realized by substituting specific residues in RocA's binding pockets of eIF4A and DDX3.

2.4. Discussion

The direct targeting of DDX3 in addition to eIF4A1/2 provides us a better understanding of how RocA targets cancer cells. However, previous efforts failed to discover the DDX3, which was possibly caused by the complicated characteristics of RocA. For example, a previous study applying biotinylated RocA in the mammalian system to look for its targets failed to find DDX3 (*65*), probably because of the absence of polypurine RNAs which enhance the binding between DDX3 and RocA. Besides that, the stronger binding between eIF4A and RocA may compete for DDX3's targeting, which explained why the DDX3 was failed to be read out in the yeast

screening (*61*), and yeast was also proved to harbor much more Tif1 (eIF4A1) and Tif2 (eIF4A2) than Ded1 (DDX3) (*92*).

Except for the importance of polypurine RNAs in the survey of RocA alternative targets, the more complex structure of DDX3 might also mask its discovery. For example, DDX3 contains long N- and C- terminal domains in addition to the conserved helicase core with eIF4A. In detail, the N-terminus of DDX3X contains nuclear export signal (NES) (*93-95*), whereas C-terminus contains arginine/serine-like (RS-like) domain which could interact with the nuclear export receptor (*94, 96*). These functions relying on the translocation of DDX3 to a specific domain, possibly limit the efficiency of RocA's targeting as well.

More recently, DEAD-box proteins like DDX3 with unstructured tails tend to enter liquid-liquid phase separation by forming phase-separated droplets. However, proteins like eIF4A that lack unstructured tails will not (*97*). In addition, DDX3 is known to be modulated by phosphorylation at multiple sites (*98*), and the deficiency of DDX3X phosphorylation fails to stimulate type-I interferon (IFN) in response to pathogens (*99*). The discriminative role of DDX3 and eIF4A, and DDX3's engagement in phase separation might also mask DDX3's discovery by RocA and suggest the complexities of RocA's functionality.

Despite the bottleneck previous studies came across, we successfully applied *O*-NBD to exploring RocA's targets by conjugating RocA to *O*-NBD. The firsthand labeling of RocA-*O*-NBD dramatically simplifies the identification of RocA's targets, which could get rid of the multi-step purification as biotinylated RocA. Also, the biotin conjugated with RocA possibly hampers the RocA's binding with some fragile components such as DDX3 and so on. This optimal application of RocA-*O*-NBD assists us in identifying DDX3 directly.

Given only Gln360 in DDX3 shows resistance to RocA's clamping, and the critical mutation (Phe163) in eIF4A1 does not attribute DDX3's resistance to RocA in the same position (Val328Leu). Therefore, there is probably a conformation difference between DDX3·RocA and eIF4A·RocA. Simply speaking, RocA likely interacts with DDX3 in a similar but not the same angle **as** estimated from the structure **(Figure 2.4)**.

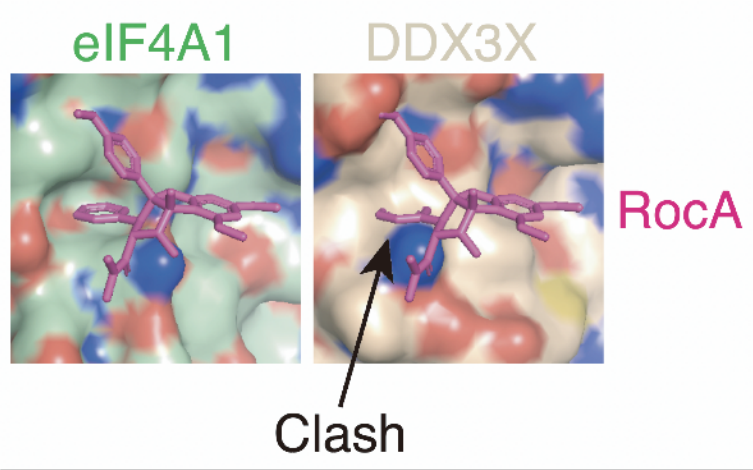

Figure 2.4. Estimated structure of RocA's binding to left) eIF4A1 and right) DDX3X. Takuhiro Ito performed this estimation.

Except for the engagement of RocA in the block of the translation scanning, it was also reported there might be a trans bystander effect induced by sequestration of eIF4A. The complexation of eIF4F by eIF4A's sequestration would reduce the availability of active mRNAs for translation initiation (*74*). Similarly, because of the essential role of DDX3 in translation initiation (*35*), similar sequestration effects possibly happen too. However, DDX3 was reported to prefer mRNAs with more complex 5' UTR (*100*), so if there is any subtle difference between DDX3 and eIF4A requires further illustrations. In addition, DDX3X has a paralog DDX3Y expressed in some specific cells, mainly male germ cells. This high sequence

similarity (about 90%) between DDX3X and DDX3Y indicates that RocA can probably also target DDX3Y (*101*).

However, there are also several paralogs of DDX3 in plants as reported before. The DDX3 transcriptome of *Aglaia* probably includes all the possible paralogs of DDX3, which might explain the limited distribution of identified Gln. In addition, another kind of plant, *Arabidopsis,* expresses three paralogs of DDX3: RH11, RH37, and RH52, and these paralogs express differentially among different tissues (*102, 103*). Thus, I assume the organs which produce specific DDX3 paralogs possibly do not produce rocaglates. However, these parts of RNAs are still sequenced and indistinguishably assembled by us, which thus leads to the detection of DDX3 isoforms without RocA-resistant mutation Gln360 **(Also see Figure 2.3.1.1)**.

Furthermore, DDX3 is easily mutated in a wide range of cancer cells, and its functionality is tightly related to tumor development (*104-106*). Also, overexpression of DDX3 is a hallmark for some cancer cells (*106*). Combining with the dominant-negative effects of RocA we presented, these types of cancer cells are predictably more sensitive to RocA.

In summary, the discovery of RocA's alternative targets DDX3, clarification of its mechanisms, and resistance give us a better understanding of its potential application into clinical therapy. However, there is remaining work to understand RocA's targeting to DDX3. The primary mechanism that requires to be clarified is how RocA precisely targets DDX3, which can be solved by resolving the 3D structure of DDX3·RocA·RNA. However, considering the relatively weak affinity between DDX3 and RNAs or RocA, this might be more challenging than eIF4A. In addition, because RocA does not simply phenocopy the inhibition of DDX3 but presents the dominant-negative inhibition, it is difficult to directly detect the translational

targets of DDX3 from Ribo-Seq data (Ribo-Seq only provides the information of ribosome-protected fragments after RocA treatment). However, I assume some experiments could answer this question by using more direct methods like performing RIP-Seq (RNA-immunoprecipitation sequencing) of DDX3 (*73*).

Chapter 3-4 (pp. 46 to 67) of my doctoral thesis cannot be made public on the Internet for 5 years from the date of doctoral degree conferral because that part has been accepted for publication.

5. Methods

5.1. Recombinant proteins' purification

The plasmids of interest are transfected into *E. coli* BL 21 cells and cultivated to OD of 0.4 ~ 0.6 in 1 L of LB medium. Following chilling the cells at 4 ℃ for half an hour, the culture is induced by adding 1 mM IPTG and cultivated overnight at 15 ℃. The pellets of *E. coli* are collected by centrifugation at 2280 x g for 30 min, flash-frozen at liquid nitrogen, and stored at - 80 ℃ before use.

The collected pellets are lysed by lysis buffer (20 mM HEPES-NaOH pH 7.5, 500 mM NaCl, 10 mM imidazole, 10 mM β-mercaptoethanol, and 0.5% NP-40) and homogenized by sonication. After centrifugation at 10,000 x g for 20 min, the supernatant is gathered to incubate with 3 mL of Ni-NTA Agarose beads (Qiagen) for 1 hr at 4 ℃. Following two times of washes with high-salt wash buffer (20 mM HEPES-NaOH pH 7.5, 1 M NaCl, 20 mM imidazole, and 10 mM β-mercaptoethanol) and one-time wash with low-salt wash buffer (20 mM HEPES-NaOH pH 7.5, 10 mM NaCl, 20 mM imidazole, and 10 mM β-mercaptoethanol). Finally, the proteins are eluted into 8 mL of elution buffer (20 mM HEPES-NaOH pH 7.5, 10 mM NaCl, 250 mM imidazole, 10 mM β -mercaptoethanol, and 10% glycerol) for further HPLC purification.

For HPLC, an NGC chromatography system (Bio-Rad) was used. The eluted proteins from Agarose beads are loaded onto the Hi-Trap Heparin HP column (GE Healthcare) and fractionated by a gradient created by mixing buffer A (20 mM HEPES-NaOH pH 7.5, 10 mM NaCl, 10% glycerol, and 1 mM DTT) and buffer B (buffer A with 1 M NaCl). The fractions

showing high peak were gathered into the storage buffer (20 mM HEPES-NaOH pH 7.5, 150 mM NaCl, 10% glycerol, and 1 mM DTT) and concentrated by Vivaspin 6 (10 kDa MWCO) (Sartorius) or Amicon Ultra-4 (10 kDa MWCO) (Millipore). All concentrated proteins are stored at -80 ℃ for further use.

5.2. Preparation of reporter mRNA

Renilla-luciferase mRNA reporter with CAA repeats or AGAGAG repeats was synthesized as before (*73*). The linearized DNA template with T7 promoter used for *in vitro* transcription was PCR-amplified from related plasmids. Then the reporter mRNA is transcribed using T7-Scribe Standard RNA IVT Kit (CELLSCRIPT) as listed below:

Components	**Amount**
RNase-Free Water	X μL
Linearized template DNA with T7 RNAP promoter	1 μg
10X T7-Scribe Transcription Buffer	2 μL
100 mM ATP	1.5 μL
100 mM CTP	1.5 μL
100 mM UTP	1.5 μL
100 mM GTP	1.5 μL
100 mM DTT	2 μL
ScriptGuard RNase Inhibitor	0.5 μL
T7-Scribe Enzyme Solution	2 μL
Total Reaction Volume	**20 μL**

The RNAs were then capped by ScriptCap m^7G Capping System following:

1). Denature *in vitro* transcribed RNA

Set up the reaction below and incubate at 65 ℃ for 5-10 minutes, then transfer to ice.

Component	Amount
RNase-Free Water	x µL
In vitro transcribed RNA, 50-60 µg	≤ 68.5 µL
Total Volume	**68.5 µL**

2). Capping reaction

Before starting the reaction, add the ScriptCap Capping Enzyme and denatured RNAs to the reaction listed below, and incubate the reaction at 37 ℃ for 30 minutes.

Component	Amount
10X ScriptCap Capping Buffer	10 µL
10 mM GTP	10 µL
2 mM SAM (freshly diluted from 20 mM stock)	5 µL
ScriptGuard RNase Inhibitor	2.5 µL
ScriptCap Capping Enzyme (10 U/µl)	4 µL
Heat-denatured RNA (from step 1)	68.5 µL
Total Reaction Volume	**100 µL**

The capped RNAs were polyadenylated by A-Plus Poly(A) Polymerase Tailing Kit (CELLSCRIPT). In detail, the capped RNAs were denatured at 65 ℃ for 5-10 minutes and vacuum concentrated until the volume was below 75.5 μL. After that, the sample was transferred to ice and then for poly(A) tailing reaction as listed below.

Component	Amount
10x A-Plus Poly(A) Tailing Buffer	10 μL
10 mM ATP	10 μL
ScriptGuard RNase Inhibitor (Sold separately)	2.5 μL
A-Plus Poly(A) Polymerase	2 μL
Heat-denatured RNA	75.5 μL
Total Reaction Volume	**100 μL**

Incubate the above reaction at 37 ℃ for 60 minutes and purify the RNA by AGENCOURT RNAclean XP beads (Beckman Coulter Life Sciences) following the manufacturer's instructions. In detail, 100 μL of samples were mixed with 180 μL (1.8 x (reaction volume)) Agencourt RNAClean XP beads thoroughly by gentle pipetting ten times. Then the reaction was placed onto a magnet plate for 5 - 10 minutes until the beads were separated from the solution. After removing the cleared solution from the reaction, 200 μL of 70% ethanol was dispensed to the sample and incubated for 30 seconds to wash the beads. This 70% ethanol wash step was repeated three times by removing all the ethanol from the bottom of the well. Finally, the beads were air-dried for 10 minutes until all visible traces of ethanol were

evaporated. Next, 40 μL of RNase-free water was used to elute the RNAs by pipetting mix 10 times.

5.3. *In vitro* translation in rabbit reticulocyte lysates

Rabbit reticulocyte lysate system (Promega) was used in this study for *in vitro* translation. The constituent of reactions contains 5 μL of lysate, 2 μL of H_2O, 1 μL of RocA or RocA-O-NBD dissolved in 1% DMSO, 1 μL of 500 nM mRNA reporter, and 1 μL of premix [100 μM Amino Acid Mixture Minus Methionine (Promega), 100 μM Amino Acid Mixture Minus Leucine (Promega), and 1 U/μL ScriptGuard RNase Inhibitor (CELLSCRIPT)]. The translation reaction was incubated at 30 ℃ for 1 hr.

To test the dominant-negative effects of RocA on translation, 1.3 μL of lysate, 4.2 μL of dilution buffer (20 mM HEPES-NaOH pH 7.5, 10 mM NaCl, 25 mM KCl, 1.1 mM $MgCl_2$, and 1 mM DTT), 2.5 μL of purified recombinant proteins dissolved in storage buffer, 0.5 μL of 20 μM RocA dissolved in 2% DMSO, 1 μL of 50 nM mRNA reporter, and 0.5 μL of 2 x premix [200 μM Amino Acid Mixture Minus Methionine (Promega), 200 μM Amino Acid Mixture Minus Leucine (Promega), and 2 U/μL ScriptGuard RNase Inhibitor (CELLSCRIPT)] were mixed and incubated at 30 ℃ for 30 min. 30 μL of 1 x Passive Lysis Buffer (Promega) was used to quench the reaction. Finally, 10 μL of the quenched mixture was transferred into 96-well white assay plate (Costar) and illuminated by *Renilla*-Glo Luciferase Assay System (Promega). GloMax Navigator (Promega) was used for detecting luminescence.

5.4. Labeling reaction of RocA-*O*-NBD

For DDX3X labeling, 20 μL of reaction consisted of 10 μM DDX3X core WT, Gln360Pro, or Gln360Leu protein; 50 μM 5' FAM-labeled RNA oligonucleotides; and 10 μM RocA or RocA-*O*-NBD in 20 mM HEPES-NaOH pH 7.5, 150 mM NaCl, 10% glycerol, 1 mM DTT, 1 mM $MgCl_2$, and 1 mM AMP-PNP was incubated at 37 ℃ for 15 min, stopped at 4 ℃. In eIF4A1 labeling, 10 μM RNA was added and incubated for 5 min.

The reaction was mixed with 125 mM Tris-HCl (pH 7.5) and subsequently loaded for SDS-PAGE. Following fixation with 50% methanol and 7% acetic acid, the fluorescence was checked by PharosFX imager (Bio-Rad). Finally, the total protein was inspected by staining the gel with Coomassie Brilliant Blue.

5.5. Western blotting

All the antibodies used in this study are listed in the “Main materials and providers” section, and all the images from this study are processed and saved by ODYSSEY CLx (LI-COR Biosciences).

5.6. Knockdown by siRNA and cell viability test

Two x 10^4 cells were seeded into 24-well plates one day before transfection. 55 nM DDX3X-specific siRNA (Dharmacon, L-006874-02-0005), eIF4A2-specific siRNA (Dharmacon, L-

013758-01-0005), and/or control siRNA (Dharmacon, D-001206-13-05) were transfected into cells using *Trans*IT-X2 Transfection Reagent System (Mirus). Four x 10^3 of the above cells are transferred to a new 96-well microplate and incubated for another 6 h. siRNA knockdown described above was repeated. Following 24 h of incubation, RocA or DMSO was added to the plate and incubated for 48 h. The cell viability was checked by RealTime-Glo MT Cell Viability Assay System (Promega). For data processing, the DMSO-treated group was used as a control for normalization by Igor Pro 8 (WaveMetrics).

5.7. Bind-n-Seq

The Dynabeads M-270 Streptavidin used in this study to pull down SBP-tagged proteins was pre-equilibrated using equilibration buffer (20 mM Tris-HCl pH 7.4, 150 mM NaCl, 5 mM $MgCl_2$, and 1 mM DTT) with 0.1% Triton X-100. One hundred picomoles of SBP-tagged proteins were then incubated with the equilibrated beads for 30 min. Following incubation, the protein-tethered beads were firstly treated with 2 U/μL Micrococcal Nuclease (TaKaRa) in 1 x Micrococcal Nuclease Buffer (TaKaRa), 0.5 x equilibration buffer, and 0.5% Triton X-100 in a total volume of 30 mL at 25 ℃ for 30 min. After 5 x washes with equilibration buffer containing 1% Triton X-100, 1 M NaCl, and 5 mM EGTA (pH 7.4), two times of rinse with equilibration buffer containing 0.1% Triton X-100 were conducted. The washed beads with proteins were then mixed with a 50 μM concentration of randomized 30nt-RNAs comprising 5'-**CTCTTTCCCTACACGACGCTCTTCCGATCT**-N30-**ATCGTAGATCGGAAGAGCACACGTCTGAA**-3' (in which bold letters represent DNA sequence, and N30 means randomized RNA sequence), which mixture was dissolved in the equilibration buffer with 0.1% Triton X-100, 0.33 U/ml SUPERase·In RNase Inhibitor

(Thermo Fisher Scientific), 2 mM ADP (Wako Pure Chemical Industries) and 2 mM Na_2HPO_4 with 3 mM RocA (or1%DMSO). The enriched proteins by beads were finally eluted with equilibration buffer but with 0.1% Triton X-100, 5 mM D-biotin (Invitrogen), 2 mM ADP, and 2 mM Na_2HPO_4, 3 mM RocA or 1% DMSO at 4 ℃ for 30 min. The proteins bounded RNAs were enriched using Oligo Clean & Concentrator Kit (Zymo Research) following the manufacture's manual. In the case of ATP, 1 μM RNAs were mixed with beads, and 2 mM AMP-PNP was used to replace 2 mM ADP and 2 mM Na_2HPO_4.

5.8. Ribosome profiling

After the treatment of 0.3 μM or 3 μM of RocA for 30 min, cell lysates containing 5 μg of RNAs are used for downstream library preparation. As described previously, 5 μg of RNAs were treated with 2 U/μg of RNase I for 45 min at 25 ℃ (*73, 75*) . Then sucrose cushion was used to collect ribosomes and for the subsequent electrophoresis. 26-34 nt length of RNAs were then excised from the 15% UREA gel and extracted.

After denaturing extracted RNAs at 95 ℃ for 2 minutes and cooling the sample on ice for 3 minutes, the size selected RNAs were then dephosphorylated using T4 polynucleotide kinase (PNK) (New England Biolabs) by incubating the reaction at 37 ℃ for 1 hr, the component of the reaction is described as below:

Component	Amount/μL	Final amount
Denatured RNA sample	7	NA
T7 PNK buffer (10 x)	1	1 x

T4 PNK (10 U/μL)	1	10 U
SUPERase·In (20U/μL)	1	20 U
Total Reaction Volume	**10**	**NA**

The phosphorylated samples from above were denatured again at 95 ℃ for 2 minutes and placed on ice for 3 minutes. After that, the samples were linker ligated with distinct barcodes using T4 RNA Ligase 2, truncated KQ (New England Biolabs) as below by incubating the reaction at 22 ℃ for 3 hr:

Component	Amount/μL	Final
50% (w/v) PEG-8000	7	17.5%
10 x T4 RNA ligase buffer	1	1 x
20 μM Preadenylated linker	1	1 μM
T4 RNA ligase 2, truncated KQ	1	100 U
Total Reaction Volume	**10**	**NA**

After the reaction of linker ligation, 20 μL of sample was brought up to 50 μL by adding 30 μL of RNase-free water. Then, 50 μL of sample was mixed with 100 μL of Oligo Binding Buffer from Oligo Clean & Concentrator Kit (Zymo Research) and 400 μL of ethanol. Subsequently, the mixture was loaded onto the Oligo Clean & Concentrator Kit column and centrifugated at 12,000 g at 4 ℃ for 1 minute. After washing twice with 750 μL DNA wash buffer by centrifugation at 12,000 g for 1 minute, the column was dried by centrifugation at 12,000 g for 5min. Finally, the column was placed into an RNase-free tube. Then, the RNA

was eluted into 7 μL of RNase-free water by centrifugation at 12,000 g for 1 minute at 4 ℃ for the next size selection electrophoresis.

The size-selected samples were then rRNA depleted by Ribo-Zero Gold rRNA Removal Kit (Human/Mouse/Rat) (Illumina) following manufactures' instruction and prepared for downstream reverse transcription.

In detail, 10 μL of linker ligated RNAs were firstly mixed with 2 μL of 1.25 μM reverse transcription (RT) primer (5' -(Phos)NNAGATCGGAAGAGCGTCGTGTAGGGAAAGAG(iSp18)GTGACTGGAGTTCAGACGTGTGCTC-3'), denatured at 65 ℃ for 5 minutes in a thermal cycler, and then placed on ice. The total of 12 μL denatured sample was then transcribed using transcriptase ProtoScript II (New England Biolabs) by adding the following components:

Component	**Amount/μL**	**Final**
Protoscript II buffer (5x)	4	1 x
dNTPs (10 mM)	1	0.5 mM
DTT	1	5 mM
SUPERase·In (20 U/μL)	1	20 U
Protoscript II (200 U/μL)	1	20 U
Total Volume	**8**	**NA**

Reverse transcription was performed by incubating the above reaction at 50 ℃ for 30 minutes, and the non-transcribed RNAs were digested by adding 2.2 μL of 1 M NaOH and incubating at 70 ℃ for 20 minutes. Finally, the reverse-transcribed single-stranded DNAs were

purified and concentrated using Oligo Clean & Concentrator Kit as described above. Following size-selection of transcribed DNA by electrophoresis, the samples were finally eluted into 7 µL of RNase-free water.

The reverse-transcribed products were then circularized with CircLigase II ssDNA ligase (Epicentre) using components listed below and incubated for 10 minutes at 80 ℃ in the thermal cycler.

Component	Amount/µL	Final
First-strand DNA	12	NA
CircLigase II buffer (10 x)	2	1 x
Betaine (5 M)	4	1 M
$MnCl_2$ (50 mM)	1	2.5 mM
CircLigase II (100 U/µL)	1	100 U
Total Reaction Volume	**20**	**NA**

Circularized DNA was PCR amplified using Phusion polymerase (New England Biolabs) following manufactures' instructions, enriched with appropriate PCR cycles, and indexed by forward primer (5' - AATGATACGGCGACCACCGAGATCTACACTCTTTCCCTACACGACGCTC-3') and reverse PCR Index primers. The finalized DNA libraries were finally sequenced on HiSeq 4000 platform (Illumina).

The most frequently used oligos for ribosome profiling in our lab, including linkers and PCR index, were listed below.

Linker Barcodes	Oligo Sequence
ATCGT	5' -/5Phos/NNNNNATCGTAGATCGGAAGAGCACACGTCTGAA/3ddC/-3'
AGCTA	5' -/5Phos/NNNNNAGCTAAGATCGGAAGAGCACACGTCTGAA/3ddC/-3'
CGTAA	5' -/5Phos/NNNNNCGTAAAGATCGGAAGAGCACACGTCTGAA/3ddC/-3'
CTAGA	5' -/5Phos/NNNNNCTAGAAGATCGGAAGAGCACACGTCTGAA/3ddC/-3'
GATCA	5' -/5Phos/NNNNNGATCAAGATCGGAAGAGCACACGTCTGAA/3ddC/-3'
GCATA	5' -/5Phos/NNNNNGCATAAGATCGGAAGAGCACACGTCTGAA/3ddC/-3'
TAGAC	5' -/5Phos/NNNNNTAGACAGATCGGAAGAGCACACGTCTGAA/3ddC/-3'
TCTAG	5' -/5Phos/NNNNNTCTAGAGATCGGAAGAGCACACGTCTGAA/3ddC/-3'

PCR Index	Oligo Sequence
ATCACG	5' -CAAGCAGAAGACGGCATACGAGATCGTGATGTGACTGGAGTTCAGACGTGTG-3'
CGATGT	5' -CAAGCAGAAGACGGCATACGAGATACATCGGTGACTGGAGTTCAGACGTGTG-3'
TTAGGC	5' -CAAGCAGAAGACGGCATACGAGATGCCTAAGTGACTGGAGTTCAGACGTGTG-3'
TGACCA	5' -CAAGCAGAAGACGGCATACGAGATTGGTCAGTGACTGGAGTTCAGACGTGTG-3'
ACAGTG	5' -CAAGCAGAAGACGGCATACGAGATCACTGTGTGACTGGAGTTCAGACGTGTG-3'
GCCAAT	5' -CAAGCAGAAGACGGCATACGAGATATTGGCGTGACTGGAGTTCAGACGTGTG-3'
CAGATC	5' -CAAGCAGAAGACGGCATACGAGATGATCTGGTGACTGGAGTTCAGACGTGTG-3'
ACTTGA	5' -CAAGCAGAAGACGGCATACGAGATTCAAGTGTGACTGGAGTTCAGACGTGTG-3'
GATCAG	5' -CAAGCAGAAGACGGCATACGAGATCTGATCGTGACTGGAGTTCAGACGTGTG-3'
TAGCTT	5' -CAAGCAGAAGACGGCATACGAGATAAGCTAGTGACTGGAGTTCAGACGTGTG-3'
GGCTAC	5' -CAAGCAGAAGACGGCATACGAGATGTAGCCGTGACTGGAGTTCAGACGTGTG-3'
CTTGTA	5' -CAAGCAGAAGACGGCATACGAGATTACAAGGTGACTGGAGTTCAGACGTGTG-3'

5.9. Data processing

5.9.1. Analysis of ribosome profiling data

Raw reads of ribosome profiling were processed as described before (*73, 75, 89*). In details, the raw sequencing data was 1) preprocessed firstly using following commands:

zcat /path/to/raw/sequencing/data/*.fastq.gz |

fastq_illumina_filter --keep N -v |

fastx_clipper -Q33 -a [adapter sequence] -c -v -o [output filename].fastq

Then the preprocessed reads were 2) split by linker barcodes using commands listed below:

fastx-split -o [output directory] -p NN -x NNNNNIIIII --min-insert=18 -s [.csv file contains sample and linker barcode information] [output filename]. fastq

The split samples were 3) aligned to noncoding RNA reference using Bowtie short-read alignment program, and the aligned reads were discarded, and unaligned reads were collected.

bowtie2 -p 8 --very-sensitive --quiet --un [output filename].nortrna.fq -x [Reference non-coding genome] -U [input file location] | rrna-stats -o [output directory for stats file] --tam --lenrange 18,51 –

After non-coding RNAs removal, the non-rRNA sequencing reads were 4) aligned to a genomic reference.

tophat -p 6 --bowtie1 --no-novel-juncs --output-dir [output directory] --GTF [reference gtf file location] [reference files] [output filename].nortrna.fq

Finally, the mapped reads were extracted by tool “samtools view”, indexed by tool “samtools index”, and deduplicated by the tool “bam-suppress-duplicates”.

samtools view -b [directory of mapped files]/accepted_hits.bam > [output filename].bam

samtools index [output filename].bam

bam-suppress-duplicates -i [indexed filename].bam -o [output filename]_unique.bam --annotate --stats=[stats filename]_duplicate_stats.txt

As a normalization, the reads mapped to mitochondria were separately extracted by using the mitochondria genome as a reference. The translation change caused by RocA was calculated by DESeq (*126*) and renormalized to total mitochondria reads (*73*).

5.9.2. Analysis of Bind-n-Seq data

The enriched motifs were defined by mean + 2S.D. and calculated as described previously (*73, 85*). To improve calculation accuracy, duplicated identical sequences are removed because of the high diversity of randomized RNAs using the following command:

fastx_collapser -Q33 -i [input filename].fq -o [output filename].fa

To confirm the quality of Bind-n-Seq, the sequenced reads are processed by removing adapters, linkers, and RT primers for quantifying the length distribution of randomized RNA sequences. The command of removing unrelated sequences is illustrated in 5.9.1. The enriched motifs were visualized using the "seqLogo" package in R.

5.10. Generation of RocA-*O*-NBD

The workflow and buffer conditions for synthesizing RocA-*O*-NBD were set and performed by Koichi Fujiwara, Mikiko Sodeoka, and Kosuke Dodo. Briefly speaking, RocA propargyl amide derivatives were generated from RocA derivative aglafoline (MedChem Express) by following the route as below **(Figure 5.10)**.

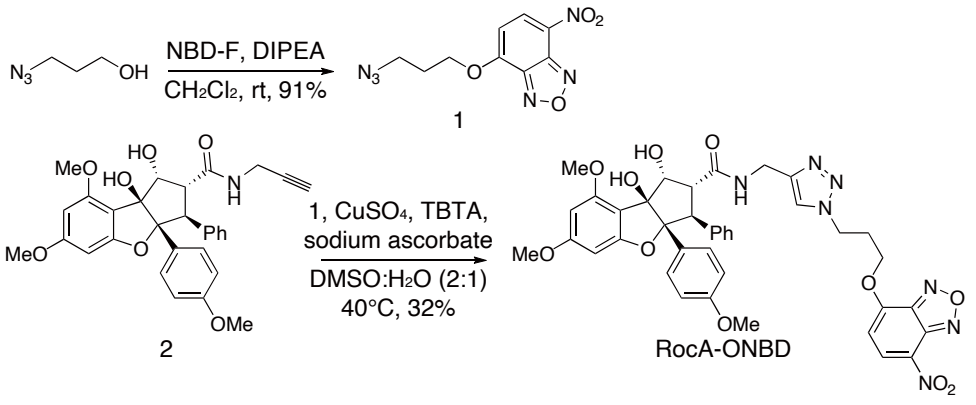

Figure 5.10. Synthesis of RocA-*O*-NBD.

5.11. Mass spectrometry

The mass spectrometry used for this study was performed by Miwako Asanuma and partially described as previously (*83*). Therefore, this study's main steps for mass spectrometry analysis can be explained as following several steps.

For identification of RocA-targets, the RocA-*O*-NBD labeled proteins from the gel are digested and immunopurified. To survey the labeling residue of RocA-*O*-NBD, the recombinant proteins are mixed with RocA-*O*-NBD and in-solution digested and immunopurified. For immunopurification of RocA-*O*-NBD labeled samples, the anti-NBD antibodies are conjugated and enriched by Protein G Mag Sepharose beads (GE Healthcare). The equipment of mass spectrometry and data processing were explained as before (*118*).

5.12. RNA-Seq and *de novo* transcriptome assembly

Ryan Muller and Shintaro Iwasaki did this part of the work. Fungi on the stem of *Aglaia* odorata (grown in Berkeley, California) was harvested and subjected to RNA extraction with hot phenol. After further chloroform extraction, RNA was subjected to rRNA depletion by Ribo-Zero Gold rRNA Removal Kit (Yeast) (Illumina). RNA-Seq library was generated by TruSeq Stranded mRNA kit (Illumina) and sequenced by HiSeq4000 (Illumina) with a pair-end 100-bp option.

The transcriptome assembly and functional annotation were performed as described previously by using Trinity and Trinotate (*75*). The eIF4A and DDX3 homolog sequences were aligned with MUSCLE (https://www.ebi.ac.uk/Tools/msa/muscle/) and depicted by ESPript 3.0 (http://espript.ibcp.fr/ESPript/ESPript/). eIF4A and DDX3 homolog sequences of model species were obtained from Uniprot. For *Ophiocordyceps* species, *Tolypocladium* species, and *Colletotrichum* orbiculare, the ORF databases were obtained from EnsemblFungi (https://fungi.ensembl.org/index.html) or Ohm laboratory (http://fungalgenomics.science.uu.nl). The closest homologs registered in Uniprot were searched by blastp (https://ftp.ncbi.nlm.nih.gov/blast/executables/blast+/LATEST/) for all the proteins in the databases to survey the eIF4A and DDX3 homologs in each species.

5.13. Phylogenetic analysis

Naoyoshi Kumakura and Shintaro Iwasaki performed the phylogenetic analysis. To identify the genus of the *Aglaia* fungus, the closely related species were predicted. *De novo* assembled transcriptome sequence of the *Aglaia* fungus was searched by BLASTn using the *Colletotrichum* aotearoa ICMP 18537 internal transcribed spacer (ITS) sequence (GenBank accession: NR_120136) (*127*) as a query. Using the best hit sequence as a query, BLASTn was performed against NCBI nucleotide collection (nr/nt), and the top 27 best hits belonged to the *Ophiocordyceps* species. To confirm this, a multilocus phylogenetic analysis of the *Aglaia* fungus with *Ophiocordyceps* species was performed. A total of 66 isolates was used for phylogenetic analysis, including an *Aglaia* fungus, 61 previously classified *Ophiocordyceps* strains consisting of 52 species, and 4 *Tolypocladium* species as outgroups. DNA sequences of ITS, small subunit ribosomal RNA (SSU), large subunit rRNA (LSU), translation elongation

factor 1-alpha (TEF1a), and RNA polymerase II largest subunit (RPB1) were used as previously reported for the classification of *Ophiocordyceps* species (*128*). Additional genomic sequences of *Ophiocordyceps* species identified by BLASTn were supplemented to the analysis. A phylogenetic tree was calculated following previously described methods (*128, 129*). Each locus (ITS, SSU, LSU, TEF1α, and RPB1) of 66 isolates (*111, 128, 130-145*) were aligned using MAFFT version 7 (*146*) and trimmed by trimAl (*147*) with an automated setting. The processed sequences obtained from every 66 isolates were concatenated by MEGA7 (*148*) to generate sequences comprising 3,782 nucleotide positions with gaps. Then, concatenated sequences were used for a maximum-likelihood analysis in RAxML version 8.2.12 (*149*) using GAMMA+P-Invar Model with 1,000 bootstrap replicates. The tree was visualized in iTOL (https://itol.embl.de/).

5.14. Monolith analysis

Mari Takahashi and Takuhiro Ito performed the monolith analysis. According to the manufacturer's protocol, the study of microscale thermophoresis was done with the Monolith NT.115 (NanoTemper) at 23 ℃. The fluorescent labeling of recombinant proteins was done with a fluorescent dye following Monolith His-Tag Labeling Kit RED-tris-NTA (NanoTemper). The final concentration of proteins was adjusted to 50 nM. After adding 50 µM of $(AG)_5A$ (Fasmac, Japan) and 2.5 mM of AMP-PNP solutions, the resultant recombinant proteins, RNA, and AMP-PNP mixture was titrated with RocA in PBS (-) buffer (Nacalai Tesque) with 5 mM $MgCl_2$, 1 mM DTT, and 0.05% Tween-20. Each group of the experiment was repeated three times.

6. Materials

6.1. Plasmids

The plasmids of pColdI-DDX3X helicase core WT, Pro324Thr, Val328Leu, Gln360Pro, Gln360Leu, and Arg363Asn are generated by inserting a DNA fragment into the backbone pColdI (TaKaRa) downstream of the His-tag with In-Fusion HD (TaKaRa). The inserting fragment of DDX3X helicase core (amino acids 132-607) was PCR amplified from HeLa cDNA, and the mutations: Pro324Thr, Val328Leu, Gln360Pro, Gln360Leu, and Arg363Asn were induced by site-direct mutagenesis.

Regarding eIF4A1 related plasmids, the human pColdI-eIF4A1 WT and Phe163Leu-Ile199Met (with *Aglaia* mutations) have already been used and reported before (*75*). To construct pColdI-eIF4A2 WT, the eIF4A2 fragment was cloned from HeLa cDNA and inserted into the pColdI backbone. In the case of pColdI-*Aglaia* fungus eIF4A, the cDNA of *Aglaia* Fungus's eIF4A was firstly reverse-transcribed from *Aglaia* fungus's total RNAs using ProtoScript II Reverse Transcriptase (New England Biolabs) and Random Primer (nonadeoxyribonucleotide mix: pd(N)9) (TaKaRa). Then, the *Aglaia* fungus eIF4A iso4 fragment was PCR-amplified from its cDNA and inserted into the pColdI backbone with His-tag. All the mutations for eIF4A related plasmids were induced by site-direct mutagenesis.

The plasmids used for Bind-n-Seq, such as pColdI-SBP-eIF4A1 and pColdI-SBP-DDX3X helicase core, were constructed mainly by adding SBP tag. For example, the SBP-eIF4A1 fragment was cloned from a reported plasmid pcDNA5/FRT/TO-SBP-eIF4A1 (*73*) and

inserted into the pColdI backbone. The DDX3X helicase core was described above and then inserted into the pColdI-SBP backbone using In-Fusion enzyme (TaKaRa).

6.2. Cell lines

The cell lines used in this study, including T-Rex-293 (HEK293) cells (Thermo Fisher Scientific) and T-REx293 SBP-eIF4A1 (Phe163Leu-Ile199Met*) eIF4A1*^{em1SINI} cells (*75*), were cultured in DMEM (13) + GlutaMAX-I (Thermo Fisher Scientific) supplemented with 10% FBS. In addition, the cancer cell line Hs 936.T and A375 cells (American Type Culture Collection, ATCC) were grown in high-glucose DMEM (Nacalai Tesque) with 10% FBS; and NCI-H1650 and NCI-H520 cells (ATCC) were grown in RPMI 1640 medium (Thermo Fisher Scientific).

6.3. Strain

The *E. coli* BL21 Star (DE3) strain (Thermo Fisher Scientific) used for recombinant proteins' purification was transformed with plasmids of interest and grown in LB medium with ampicillin at 37 ℃ for the enrichment of expressed proteins.

6.4. Main materials and providers

The primary materials used in this study are listed as below:

6.4.1. Antibodies

Rabbit monoclonal anti-NBD antibody	Acris Antibodies GmbH	Cat#BP086; RRID: AB_972399
Mouse monoclonal Anti-pan-eIF4A antibody	Santa Cruz Biotechnology	Cat#sc-377315; RRID: AB_2868449
Rabbit polyclonal anti-eIF4A1 antibody	Cell Signaling Technology	Cat#2490S; RRID: AB_823487
Rabbit polyclonal anti-eIF4A2 antibody	Abcam,	Cat#ab31218; RRID: AB_732123
Mouse monoclonal anti-β-actin antibody	LI-COR Biosciences	Cat#926–42212; RRID: AB_2756372
Rabbit monoclonal anti-DDX3X antibody	Cell Signaling Technology	Cat#8192S; RRID: AB_10860416
Goat polyclonal anti-rabbit IgG antibody conjugated with IRDye 800CW	LI-COR Biosciences	Cat#926–32211; RRID: AB_621843
Goat polyclonal anti-mouse IgG antibody conjugated with IRDye800CW	LI-COR Biosciences	Cat#926–32210; RRID: AB_621842

6.4.2. Bacterial strain

E. coli: BL21 Star (DE3)	Thermo Fisher Scientific

6.4.3. Chemicals, Peptides, and Recombinant Proteins

Rocaglamide A	Sigma-Aldrich
Aglafoline	MedChem Express
RocA-*O*-NBD	This study
Adenylyl-imidodiphosphate (AMP-PNP)	Roche
ADP	Wako Pure Chemical Industries
D-biotin	Invitrogen
Distilled water containing 0.1% (v/v) formic acid (FA)	Kanto Chemical Co., Inc.
Recombinant protein: His-DDX3X helicase core WT	This study
Recombinant protein: His-DDX3X helicase core Pro324Thr	This study
Recombinant protein: His-DDX3X helicase core Val328Leu	This study
Recombinant protein: His-DDX3X helicase core Gln360Pro	This study
Recombinant protein: His-DDX3X helicase core Gln360Leu	This study

Recombinant protein: His-DDX3X helicase core Arg363Asn	This study
Recombinant protein: His-DDX3X full length	This study
Recombinant protein: His-eIF4A1 WT	Iwasaki *et al.* 2019
Recombinant protein: His-eIF4A1 Phe163Leu-Ile199Met	Iwasaki *et al.* 2019
Recombinant protein: His-eIF4A2 WT	This study
Recombinant protein: His-SBP-eIF4A1	This study
Recombinant protein: His-SBP-DDX3X helicase core	This study
Recombinant protein: His-eIF4A1 WT Phe163Gly	This study
Recombinant protein: His-*Aglaia* fungus eIF4A1 WT	This study
Recombinant protein: His-*Aglaia* fungus eIF4A1 Gly172Phe	This study
Sequencing Grade Modified trypsin	Promega
Lysyl endopeptidase (Mass Spectrometry Grade)	FUJIFILM Wako Chemical
RNase I	Epicentre

6.4.4. Assays

DMEM (1×) + GlutaMAX-I	Thermo Fisher Scientific
High Glucose DMEM	Nacalai Tesque
RPMI 1640 Medium	Thermo Fisher Scientific
Ni-NTA Agarose	Qiagen
HiTrap Heparin HP column 1 ml	GE Healthcare
NAP-5	GE Healthcare
PD-10	GE Healthcare
Vivaspin 6, 10 kDa MWCO	GE Healthcare
Amicon Ultra-4, 10 kDa MWCO	Millipore
T7-Scribe Standard RNA IVT Kit	CELLSCRIPT
ScriptCap m^7G Capping System	CELLSCRIPT
ScriptCap 2′-*O*-Methyltransferase Kit	CELLSCRIPT
A-Plus Poly(A) Polymerase Tailing Kit	CELLSCRIPT
Rabbit Reticulocyte Lysate System, Nuclease Treated	Promega
Renilla-Glo Luciferase Assay System	Promega
MicroSpin G-25 Column	GE Healthcare
Dynabeads Protein G	Thermo Fisher Scientific
Protein G Mag Sepharose beads	GE Healthcare
MonoSpin C18 S	GL Science
TransIT-X2 Transfection Reagent System	Mirus
RealTime-Glo MT Cell Viability Assay System	Promega
Monolith His-Tag Labeling Kit RED-tris-NTA	NanoTemper

Dynabeads M-270 Streptavidin	Thermo Fisher Scientific
Oligo Clean & Concentrator Kit	Zymo Research
Ribo-Zero Gold rRNA Removal Kit (Human/Mouse/Rat)	Illumina

6.4.5. Deposited data

Ribosome profiling of cancer cell lines with RocA treatment, raw, and processed data	GEO: GSE148636
RNA-Bind-n-Seq of eIF4A1 and DDX3X with RocA treatments, raw and processed data	GEO: GSE150111

6.4.6. Cell lines

T-Rex-293 (HEK)	Thermo Fisher Scientific
T-REx293 SBP-eIF4A1 (Phe163Leu-Ile199Met) *eIF4A1*^{SINI}	Iwasaki *et al.* 2019
Hs 936.T	American Type Culture Collection (ATCC)
A375	American Type Culture Collection (ATCC)
NCI-H1650	American Type Culture Collection (ATCC)
NCI-H520	American Type Culture Collection (ATCC)

6.4.7. Oligonucleotides

FAM labeled RNA $(AG)_{10}$: FAM-AGAGAGAGAG AGAGAGAGAG	Hokkaido System Science, Iwasaki *et al.* 2019
FAM labeled RNA $(UC)_{10}$: FAM-UCUCUCUCUCUCUCUCUCUC	Hokkaido System Science, This paper
$(AG)_5$A: AGAGAGAGAGA	Fasmac, This paper
DDX3X-specific siRNA	Dharmacon
eIF4A2-specific siRNA	Dharmacon
control siRNA	Dharmacon
CTCTTTCCCTACACGACGCTCTTCCGATC T-N_{30}-	Gene Design

ATCGTAGATCGGAAGAGCACACGTCTGA
A (letters in bold represent the DNA sequence and
N represents random the RNA sequence)

6.4.8. Recombinant DNA

pColdI-DDX3X helicase core WT	This study
pColdI-DDX3X helicase core Pro324Thr	This study
pColdI-DDX3X helicase core Val328Leu	This study
pColdI-DDX3X helicase core Gln360Pro	This study
pColdI-DDX3X helicase core Gln360Leu	This study
pColdI-DDX3X helicase core Arg363Asn	This study
pColdI-eIF4A1 WT	Iwasaki *et al.* 2019
pColdI-eIF4A1 Phe163Gly	This study
pColdI-eIF4A1 Phe163Leu-Ile199Met	Iwasaki *et al.* 2019
pColdI-eIF4A2 WT	This study
pColdI-SBP-eIF4A1	This study
pColdI-SBP-DDX3X helicase core	This study
psiCHECK2-CAA repeats	Iwasaki *et al.* 2016
psiCHECK2-7×AGAGAG motifs	Iwasaki *et al.* 2016
pColdI-*Aglaia* fungus eIF4A1 Gly172Phe	This study
pColdI-*Aglaia* fungus eIF4A1 WT	This study

6.4.9. Software

Igor Pro Version: 8.01	WaveMetrics

6.4.10. Others

NGC chromatography system	Bio-Rad
GloMax Navigator	Promega
Image Pharos FX	Bio-Rad
ODYSSEY CLx	LI-COR Biosciences
LTQ Orbitrap XL mass spectrometer	Thermo Fisher Scientific
Infinite F-200 PRO	TECAN
Monolith NT.115	NanoTemper

6.5. Oligonucleotides sequence

6.5.1. Plasmids

Name	Primers
pColdI-DDX3X helicase core WT	pColdI-backbone F, pColdI-backbone R, DDX3X helicase core WT F, DDX3X helicase core WT R
pColdI-DDX3X helicase core Pro324Thr	DDX3X helicase core Pro324Thr F, DDX3X helicase core Pro324Thr R
pColdI-DDX3X helicase core Val328Leu	DDX3X helicase core Val328Leu F, DDX3X helicase core Val328Leu R
pColdI-DDX3X helicase core Gln360Pro	DDX3X helicase core Gln360Pro F, DDX3X helicase core Gln360Pro R
pColdI-DDX3X helicase core Gln360Leu	DDX3X helicase core Gln360Leu F, DDX3X helicase core Gln360Leu R
pColdI-DDX3X helicase core Arg363Asn	DDX3X helicase core Arg363Asn F, DDX3X helicase core Arg363Asn R
pColdI-eIF4A1 WT	Iwasaki *et al.* 2019
pColdI-eIF4A1 Phe163Gly	eIF4A1 Phe163Gly F, eIF4A1 Phe163Gly R
pColdI-eIF4A1 Phe163Leu-Ile199Met	Iwasaki *et al.* 2019
pColdI-eIF4A2 WT	pColdI-backbone F, pColdI-backbone R, eIF4A2 WT F, eIF4A2 WT R
pColdI-SBP-DDX3X helicase core	pColdI-backbone F, pColdI-backbone R, SBP-DDX3X helicase core F, SBP-DDX3X helicase core R
psiCHECK2-CAA repeats	Iwasaki *et al.* 2016
psiCHECK2-7×AGAGAG motifs	Iwasaki *et al.* 2016
pColdI-*Aglaia* fungus eIF4A1 WT	pColdI-backbone F, pColdI-backbone R, *Aglaia* fungus eIF4A1 WT F, *Aglaia* fungus eIF4A1 WT R
pColdI-*Aglaia* fungus eIF4A1 Gly172Phe	pColdI-backbone F, pColdI-backbone R, *Aglaia* fungus eIF4A1 Gly172Phe F, *Aglaia* fungus eIF4A1 Gly172Phe R

6.5.2. Primers and templates

Primers	Templates	Sequence
pColdI-backbone F	pColdI-eIF4A1 WT	TGAAAGCTTGTCGACCTGC
pColdI-backbone R	pColdI-eIF4A1 WT	ATGCCTACCTTCGATATGATGAT
DDX3X helicase core WT F	Hela cDNA	ATCGAAGGTAGGCATGATGAAGATGAT TGGTCAAAACCAC

DDX3X helicase core WT R	Hela cDNA	CAGGTCGACAAGCTTTCAACCGCTACTTTGTCGGTAG
DDX3X helicase core Pro324Thr F	pColdI-DDX3X helicase core WT	TAGCCACTACCGGACGT
DDX3X helicase core Pro324Thr R	pColdI-DDX3X helicase core WT	TAGACGTCCGGTAGTGGC
DDX3X helicase core Val328Leu F	pColdI-DDX3X helicase core WT	ACTCCAGGACGTCTATTAGATATGAT
DDX3X helicase core Val328Leu R	pColdI-DDX3X helicase core WT	CAATCTTTCCTCTTTCCATCATATCTAATAG
DDX3X helicase core Gln360Pro F	pColdI-DDX3X helicase core WT	GGTTTGAGCCTCCGATTCG
DDX3X helicase core Gln360Pro R	pColdI-DDX3X helicase core WT	CTATTCTACGAATCGGAGGCT
DDX3X helicase core Gln360Leu F	pColdI-DDX3X helicase core WT	GGTTTGAGCCTCTGATTCGT
DDX3X helicase core Gln360Leu R	pColdI-DDX3X helicase core WT	TTCGACTATTCTACGAATCAGAGGCT
DDX3X helicase core Arg363Asn F	pColdI-DDX3X helicase core WT	GAGCCTCAGATTCGTAACATAGT
DDX3X helicase core Arg363Asn R	pColdI-DDX3X helicase core WT	CATAGTATCTTGTTCGACTATGTTACG
eIF4A1 Phe163Gly F	pColdI-eIF4A1 WT	GGCCGTGTGGGCGATAT
eIF4A1 Phe163Gly R	pColdI-eIF4A1 WT	GGTTAAGCATATCGCCCACAC
eIF4A2 WT F	Hela cDNA	ATCGAAGGTAGGCATATGTCTGGTGGCTCCG
eIF4A2 WT R	Hela cDNA	CAGGTCGACAAGCTTTTAAATAAGGTCAGCCACATTCATGGG
SBP-DDX3X helicase core F	pColdI-DDX3X helicase core WT	CCTAGCGGCGGAGGAGATGAAGATGATTGGTCAAAACCAC
SBP-DDX3X helicase core R	pColdI-DDX3X helicase core WT	ACCGAGCTCCATATGTCAACCGCTACTTTGTCGG
Aglaia fungus eIF4A1 WT F	*Aglaia* fungus cDNA	ATCGAAGGTAGGCATATGAAAAACGACGGCGACT
Aglaia fungus eIF4A1 WT R	*Aglaia* fungus cDNA	CAGGTCGACAAGCTTTTAGAGAAGATCCGCGACAGT
Aglaia fungus eIF4A1 Gly172Phe F	pColdI-*Aglaia* fungus eIF4A1 WT	ACCCCTGGACGTGTGTTT
Aglaia fungus eIF4A1 Gly172Phe R	pColdI-*Aglaia* fungus eIF4A1 WT	TTTTCAGACATTTACGGATTATCATGTCAAA

Acknowledgments

Three years of PhD studies fly like an arrow. In the happy journey to be a real PhD, I want to thank all the people I met in Japan. There is no them, and there is no me.

Firstly, I want to give my deep thanks to my supervisor and my motivation Dr. Shintaro Iwasaki. His continuous enthusiasm and always patience drive me to learn more about science and be critical of the experiments. I also want to thank Dr. Yuichi Shichino's kind mentoring and answering my questions. Mari Mito and Hironori Saito's kind support in my project also help me a lot. In addition, all the lab members in the Iwasaki lab contributed their valuable comments on the manuscript.

Secondly, I want to thank Miwako Asanuma, Koichi Fujiwara, Kosuke Dodo, and Mikiko Sodeoka's kind help in synthesizing RocA-*O*-NBD and mass spectrometry analysis. Finally, I am also grateful for Mari Takahashi's and Dr. Takuhiro Ito's support in the structural analysis and monolith analysis. Their collaborative support makes this work more significant.

In addition, I appreciate Dr. Nick Ingolia's and Dr. Stephen Floor's contributions in the very primary finding of DDX3 as a target of RocA. Although I still do not have a chance to thank them in person, I deeply respect and appreciate their suggestions and help.

I also want to thank Ryan Muller, Naoyoshi Kumakura, and everyone engaged in fungi work. All of them are excellent collaborators in guiding me to the world of the *Aglaia* fungus. There is not their contribution, and there is no such good progress in this project.

Finally, I appreciate the financial support from the program “International Program Associate” of RIKEN, which makes me more focused on my studies and research. RIKEN provides us a suitable environment for science, research, and housing. I appreciate everything that RIKEN gives us.

I also want to thank my family, parents, brothers, and sisters far from me but always stand behind me. Mainly, I am highly willing to appreciate my mother: every word of her, her patience, and every love from her make me a better person!

Reference

1. C. Vaklavas, S. W. Blume, W. E. Grizzle, Translational Dysregulation in Cancer: Molecular Insights and Potential Clinical Applications in Biomarker Development. *Front Oncol* **7**, 158 (2017).
2. J. W. Hershey, N. Sonenberg, M. B. Mathews, Principles of translational control: an overview. *Cold Spring Harb Perspect Biol* **4**, (2012).
3. A. Antoun, M. Y. Pavlov, M. Lovmar, M. Ehrenberg, How initiation factors tune the rate of initiation of protein synthesis in bacteria. *EMBO J* **25**, 2539-2550 (2006).
4. B. S. Laursen, H. P. Sorensen, K. K. Mortensen, H. U. Sperling-Petersen, Initiation of protein synthesis in bacteria. *Microbiol Mol Biol Rev* **69**, 101-123 (2005).
5. R. J. Jackson, C. U. Hellen, T. V. Pestova, The mechanism of eukaryotic translation initiation and principles of its regulation. *Nat Rev Mol Cell Biol* **11**, 113-127 (2010).
6. C. E. Aitken, J. R. Lorsch, A mechanistic overview of translation initiation in eukaryotes. *Nat Struct Mol Biol* **19**, 568-576 (2012).
7. T. V. Pestova, C. U. Hellen, The structure and function of initiation factors in eukaryotic protein synthesis. *Cell Mol Life Sci* **57**, 651-674 (2000).
8. E. D. Carlson, R. Gan, C. E. Hodgman, M. C. Jewett, Cell-free protein synthesis: applications come of age. *Biotechnol Adv* **30**, 1185-1194 (2012).
9. S. Chong, Overview of cell-free protein synthesis: historic landmarks, commercial systems, and expanding applications. *Curr Protoc Mol Biol* **108**, 16 30 11-11 (2014).

10. N. Robichaud, N. Sonenberg, D. Ruggero, R. J. Schneider, Translational Control in Cancer. *Cold Spring Harb Perspect Biol* **11**, (2019).

11. J. Pelletier, J. Graff, D. Ruggero, N. Sonenberg, Targeting the eIF4F translation initiation complex: a critical nexus for cancer development. *Cancer Res* **75**, 250-263 (2015).

12. T. V. Pestova *et al.*, Molecular mechanisms of translation initiation in eukaryotes. *Proc Natl Acad Sci U S A* **98**, 7029-7036 (2001).

13. F. Raza, J. A. Waldron, J. L. Quesne, Translational dysregulation in cancer: eIF4A isoforms and sequence determinants of eIF4A dependence. *Biochem Soc Trans* **43**, 1227-1233 (2015).

14. P. Song, F. Yang, H. Jin, X. Wang, The regulation of protein translation and its implications for cancer. *Signal Transduct Target Ther* **6**, 68 (2021).

15. Y. N. Cheung *et al.*, Dissociation of eIF1 from the 40S ribosomal subunit is a key step in start codon selection in vivo. *Genes Dev* **21**, 1217-1230 (2007).

16. D. Fijalkowska *et al.*, eIF1 modulates the recognition of suboptimal translation initiation sites and steers gene expression via uORFs. *Nucleic Acids Res* **45**, 7997-8013 (2017).

17. L. L. Maduzia, A. Moreau, N. Poullet, S. Chaffre, Y. Zhang, The role of eIF1 in translation initiation codon selection in Caenorhabditis elegans. *Genetics* **186**, 1187-1196 (2010).

18. J. S. Nanda *et al.*, eIF1 controls multiple steps in start codon recognition during eukaryotic translation initiation. *J Mol Biol* **394**, 268-285 (2009).

19. A. Thakur, A. G. Hinnebusch, eIF1 Loop 2 interactions with Met-tRNAi control the accuracy of start codon selection by the scanning preinitiation complex. *Proc Natl Acad Sci U S A* **115**, E4159-E4168 (2018).

20. F. Zhou, H. Zhang, S. D. Kulkarni, J. R. Lorsch, A. G. Hinnebusch, eIF1 discriminates against suboptimal initiation sites to prevent excessive uORF translation genome-wide. *RNA* **26**, 419-438 (2020).

21. K. Feoktistova, E. Tuvshintogs, A. Do, C. S. Fraser, Human eIF4E promotes mRNA restructuring by stimulating eIF4A helicase activity. *Proc Natl Acad Sci U S A* **110**, 13339-13344 (2013).

22. A. Batool, S. Aashaq, K. I. Andrabi, Eukaryotic initiation factor 4E (eIF4E): A recap of the cap-binding protein. *J Cell Biochem* **120**, 14201-14212 (2019).

23. W. T. Lu, A. Wilczynska, E. Smith, M. Bushell, The diverse roles of the eIF4A family: you are the company you keep. *Biochem Soc Trans* **42**, 166-172 (2014).

24. N. E. Shirokikh, T. Preiss, Translation initiation by cap-dependent ribosome recruitment: Recent insights and open questions. *Wiley Interdiscip Rev RNA* **9**, e1473 (2018).

25. J. A. Waldron, F. Raza, J. Le Quesne, eIF4A alleviates the translational repression mediated by classical secondary structures more than by G-quadruplexes. *Nucleic Acids Res* **46**, 3075-3087 (2018).

26. H. D. Ryoo, D. Vasudevan, Two distinct nodes of translational inhibition in the Integrated Stress Response. *BMB Rep* **50**, 539-545 (2017).

27. T. Adomavicius *et al.*, The structural basis of translational control by eIF2 phosphorylation. *Nat Commun* **10**, 2136 (2019).

28. C. J. Lin, R. Cencic, J. R. Mills, F. Robert, J. Pelletier, c-Myc and eIF4F are components of a feedforward loop that links transcription and translation. *Cancer Res* **68**, 5326-5334 (2008).

29. C. C. Thoreen, Many roads from mTOR to eIF4F. *Biochem Soc Trans* **41**, 913-916 (2013).

30. V. Gandin *et al.*, mTORC1 and CK2 coordinate ternary and eIF4F complex assembly. *Nat Commun* **7**, 11127 (2016).

31. F. Liu, A. A. Putnam, E. Jankowsky, DEAD-box helicases form nucleotide-dependent, long-lived complexes with RNA. *Biochemistry* **53**, 423-433 (2014).

32. C. S. Lee *et al.*, Human DDX3 functions in translation and interacts with the translation initiation factor eIF3. *Nucleic Acids Res* **36**, 4708-4718 (2008).

33. O. Cordin, J. Banroques, N. K. Tanner, P. Linder, The DEAD-box protein family of RNA helicases. *Gene* **367**, 17-37 (2006).

34. B. Phung *et al.*, The X-Linked DDX3X RNA Helicase Dictates Translation Reprogramming and Metastasis in Melanoma. *Cell Rep* **27**, 3573-3586 e3577 (2019).

35. R. Soto-Rifo *et al.*, DEAD-box protein DDX3 associates with eIF4F to promote translation of selected mRNAs. *EMBO J* **31**, 3745-3756 (2012).

36. D. Sharma, A. A. Putnam, E. Jankowsky, Biochemical Differences and Similarities between the DEAD-Box Helicase Orthologs DDX3X and Ded1p. *J Mol Biol* **429**, 3730-3742 (2017).

37. P. Schutz *et al.*, Comparative structural analysis of human DEAD-box RNA helicases. *PLoS One* **5**, (2010).

38. S. Rocak, P. Linder, DEAD-box proteins: the driving forces behind RNA metabolism. *Nat Rev Mol Cell Biol* **5**, 232-241 (2004).

39. M. Bhat *et al.*, Targeting the translation machinery in cancer. *Nat Rev Drug Discov* **14**, 261-278 (2015).

40. K. A. Urtishak *et al.*, Targeting EIF4E signaling with ribavirin in infant acute lymphoblastic leukemia. *Oncogene* **38**, 2241-2262 (2019).

41. N. Siddiqui, N. Sonenberg, Signalling to eIF4E in cancer. *Biochem Soc Trans* **43**, 763-772 (2015).

42. A. G. Duffy *et al.*, Modulation of tumor eIF4E by antisense inhibition: A phase I/II translational clinical trial of ISIS 183750-an antisense oligonucleotide against eIF4E-in combination with irinotecan in solid tumors and irinotecan-refractory colorectal cancer. *Int J Cancer* **139**, 1648-1657 (2016).

43. M. Sobocan, M. A. Smolle, C. Schatz, J. Haybaeck, The Interplay of Tumor Stroma and Translational Factors in Endometrial Cancer. *Cancers (Basel)* **12**, (2020).

44. Y. Sun *et al.*, Single-molecule kinetics of the eukaryotic initiation factor 4AI upon RNA unwinding. *Structure* **22**, 941-948 (2014).

45. M. E. Bordeleau *et al.*, Therapeutic suppression of translation initiation modulates chemosensitivity in a mouse lymphoma model. *J Clin Invest* **118**, 2651-2660 (2008).

46. M. E. Bordeleau *et al.*, Functional characterization of IRESes by an inhibitor of the RNA helicase eIF4A. *Nat Chem Biol* **2**, 213-220 (2006).

47. M. E. Bordeleau *et al.*, Stimulation of mammalian translation initiation factor eIF4A activity by a small molecule inhibitor of eukaryotic translation. *Proc Natl Acad Sci U S A* **102**, 10460-10465 (2005).

48. M. E. Bordeleau *et al.*, RNA-mediated sequestration of the RNA helicase eIF4A by Pateamine A inhibits translation initiation. *Chem Biol* **13**, 1287-1295 (2006).

49. T. L. Peters *et al.*, Target-Based Screening against eIF4A1 Reveals the Marine Natural Product Elatol as a Novel Inhibitor of Translation Initiation with In Vivo Antitumor Activity. *Clin Cancer Res* **24**, 4256-4270 (2018).

50. J. Tillotson *et al.*, ATP-competitive, marine derived natural products that target the DEAD box helicase, eIF4A. *Bioorg Med Chem Lett* **27**, 4082-4085 (2017).

51. C. Jiang *et al.*, Targeting the N Terminus of eIF4AI for Inhibition of Its Catalytic Recycling. *Cell Chem Biol* **26**, 1417-1426 e1415 (2019).

52. S. J. Yun *et al.*, The mechanistic insight of a specific interaction between 15d-Prostaglandin-J2 and eIF4A suggests an evolutionary conserved role across species. *Biol Open* **7**, (2018).

53. Y. Z. Abdelkrim *et al.*, The steroid derivative 6-aminocholestanol inhibits the DEAD-box helicase eIF4A (LieIF4A) from the Trypanosomatid parasite Leishmania by perturbing the RNA and ATP binding sites. *Mol Biochem Parasitol* **226**, 9-19 (2018).

54. G. Schulz, C. Victoria, A. Kirschning, E. Steinmann, Rocaglamide and silvestrol: a long story from anti-tumor to anti-coronavirus compounds. *Nat Prod Rep* **38**, 18-23 (2021).

55. G. Agarwal, L. S. Chang, D. D. Soejarto, A. D. Kinghorn, Update on Phytochemical and Biological Studies on Rocaglate Derivatives from Aglaia Species. *Planta Med*, (2021).

56. G. Taroncher-Oldenburg *et al.*, Targeting the DEAD-Box RNA Helicase eIF4A with Rocaglates-A Pan-Antiviral Strategy for Minimizing the Impact of Future RNA Virus Pandemics. *Microorganisms* **9**, (2021).

57. S. Santagata *et al.*, Tight coordination of protein translation and HSF1 activation supports the anabolic malignant state. *Science* **341**, 1238303 (2013).

58. G. Polier *et al.*, The natural anticancer compounds rocaglamides inhibit the Raf-MEK-ERK pathway by targeting prohibitin 1 and 2. *Chem Biol* **19**, 1093-1104 (2012).

59. J. Y. Zhu *et al.*, The traditional Chinese herbal compound rocaglamide preferentially induces apoptosis in leukemia cells by modulation of mitogen-activated protein kinase activities. *Int J Cancer* **121**, 1839-1846 (2007).

60. H. Alachkar *et al.*, Silvestrol exhibits significant in vivo and in vitro antileukemic activities and inhibits FLT3 and miR-155 expressions in acute myeloid leukemia. *J Hematol Oncol* **6**, 21 (2013).

61. H. Sadlish *et al.*, Evidence for a Functionally Relevant Rocaglamide Binding Site on the eIF4A-RNA Complex. *Acs Chemical Biology* **8**, 1519-1527 (2013).

62. F. L. An *et al.*, Cytotoxic Rocaglate Derivatives from Leaves of Aglaia perviridis. *Sci Rep* **6**, 20045 (2016).

63. J. L. Oblinger *et al.*, Components of the eIF4F complex are potential therapeutic targets for malignant peripheral nerve sheath tumors and vestibular schwannomas. *Neuro Oncol* **18**, 1265-1277 (2016).

64. R. Cencic *et al.*, Antitumor Activity and Mechanism of Action of the Cyclopenta[b]benzofuran, Silvestrol. *Plos One* **4**, (2009).

65. M. E. Bordeleau *et al.*, Therapeutic suppression of translation initiation modulates chemosensitivity in a mouse lymphoma model. *Journal of Clinical Investigation* **118**, 2651-2660 (2008).

66. T. Liu *et al.*, Synthetic Silvestrol Analogues as Potent and Selective Protein Synthesis Inhibitors. *Journal of Medicinal Chemistry* **55**, 8859-8878 (2012).

67. H. Yurugi *et al.*, A subset of flavaglines inhibits KRAS nanoclustering and activation. *J Cell Sci* **133**, (2020).

68. J. Chu *et al.*, Amidino-Rocaglates: A Potent Class of eIF4A Inhibitors. *Cell Chem Biol* **26**, 1586-1593 e1583 (2019).

69. J. T. Ernst *et al.*, Design of Development Candidate eFT226, a First in Class Inhibitor of Eukaryotic Initiation Factor 4A RNA Helicase. *Journal of Medicinal Chemistry* **63**, 5879-5955 (2020).

70. W. Zhang *et al.*, Chemical Synthesis Enables Structural Reengineering of Aglaroxin C Leading to Inhibition Bias for Hepatitis C Viral Infection. *J Am Chem Soc* **141**, 1312-1323 (2019).

71. I. H. K. Too, I. Bonne, E. L. Tan, J. J. H. Chu, S. Alonso, Prohibitin plays a critical role in Enterovirus 71 neuropathogenesis. *PLoS Pathog* **14**, e1006778 (2018).

72. J. K. Wang *et al.*, Aglaia odorata Lour. extract inhibit ischemic neuronal injury potentially via suppressing p53/Puma-mediated mitochondrial apoptosis pathway. *J Ethnopharmacol* **248**, 112336 (2020).

73. S. Iwasaki, S. N. Floor, N. T. Ingolia, Rocaglates convert DEAD-box protein eIF4A into a sequence-selective translational repressor. *Nature* **534**, 558-561 (2016).

74. J. Chu *et al.*, Rocaglates Induce Gain-of-Function Alterations to eIF4A and eIF4F. *Cell Reports* **30**, 2481-+ (2020).

75. S. Iwasaki *et al.*, The Translation Inhibitor Rocaglamide Targets a Bimolecular Cavity between eIF4A and Polypurine RNA. *Mol Cell* **73**, 738-748 e739 (2019).

76. J. Chu *et al.*, CRISPR-Mediated Drug-Target Validation Reveals Selective Pharmacological Inhibition of the RNA Helicase, eIF4A. *Cell Reports* **15**, 2340-2347 (2016).

77. C. A. Deutsch *et al.*, Increase in crop losses to insect pests in a warming climate. *Science* **361**, 916-919 (2018).

78. L. Chiarappa, H. C. Chiang, R. F. Smith, Plant pests and diseases: assessment of crop losses. *Science* **176**, 769-773 (1972).

79. L. Lo Presti *et al.*, Fungal effectors and plant susceptibility. *Annu Rev Plant Biol* **66**, 513-545 (2015).

80. A. Osbourn, P. Bowyer, P. Lunness, B. Clarke, M. Daniels, Fungal pathogens of oat roots and tomato leaves employ closely related enzymes to detoxify different host plant saponins. *Mol. Plant. Microbe. Interact.* **8**, 971-978 (1995).

81. W. M. L. Crombie, L. Crombie, J. B. Green, J. A. Lucas, Pathogenicity of 'take-all' fungus to oats: Its relationship to the concentration and detoxification of the four avenacins. *Phytochemistry* **25**, 2075-2083 (1986).

82. Y. Pareja-Jaime, M. I. G. Roncero, M. C. Ruiz-Roldán, Tomatinase from Fusarium oxysporum f. sp. lycopersici is required for full virulence on tomato plants. *Mol. Plant. Microbe. Interact.* **21**, 728-736 (2008).

83. T. Yamaguchi *et al.*, Turn-ON fluorescent affinity labeling using a small bifunctional O-nitrobenzoxadiazole unit. *Chem. Sci.* **5**, 1021-1029 (2014).

84. S. N. Floor, K. J. Condon, D. Sharma, E. Jankowsky, J. A. Doudna, Autoinhibitory Interdomain Interactions and Subfamily-specific Extensions Redefine the Catalytic Core of the Human DEAD-box Protein DDX3. *J Biol Chem* **291**, 2412-2421 (2016).

85. N. Lambert *et al.*, RNA Bind-n-Seq: quantitative assessment of the sequence and structural binding specificity of RNA binding proteins. *Mol Cell* **54**, 887-900 (2014).

86. J. Barretina *et al.*, The Cancer Cell Line Encyclopedia enables predictive modelling of anticancer drug sensitivity. *Nature* **483**, 603-607 (2012).

87. C. Klijn *et al.*, A comprehensive transcriptional portrait of human cancer cell lines. *Nat Biotechnol* **33**, 306-312 (2015).

88. G. A. Brar, J. S. Weissman, Ribosome profiling reveals the what, when, where and how of protein synthesis. *Nat Rev Mol Cell Bio* **16**, 651-664 (2015).

89. N. T. Ingolia, G. A. Brar, S. Rouskin, A. M. McGeachy, J. S. Weissman, The ribosome profiling strategy for monitoring translation in vivo by deep sequencing of ribosome-protected mRNA fragments. *Nature Protocols* **7**, 1534-1550 (2012).

90. N. T. Ingolia, S. Ghaemmaghami, J. R. Newman, J. S. Weissman, Genome-wide analysis in vivo of translation with nucleotide resolution using ribosome profiling. *Science* **324**, 218-223 (2009).

91. N. T. Ingolia, L. F. Lareau, J. S. Weissman, Ribosome profiling of mouse embryonic stem cells reveals the complexity and dynamics of mammalian proteomes. *Cell* **147**, 789-802 (2011).

92. N. A. Kulak, G. Pichler, I. Paron, N. Nagaraj, M. Mann, Minimal, encapsulated proteomic-sample processing applied to copy-number estimation in eukaryotic cells. *Nat Methods* **11**, 319-324 (2014).

93. R. Brennan *et al.*, Investigating nucleo-cytoplasmic shuttling of the human DEAD-box helicase DDX3. *Eur J Cell Biol* **97**, 501-511 (2018).

94. J. Mo *et al.*, DDX3X: structure, physiologic functions and cancer. *Mol Cancer* **20**, 38 (2021).

95. V. S. Yedavalli, C. Neuveut, Y. H. Chi, L. Kleiman, K. T. Jeang, Requirement of DDX3 DEAD box RNA helicase for HIV-1 Rev-RRE export function. *Cell* **119**, 381-392 (2004).

96. M. C. Lai, Y. H. Lee, W. Y. Tarn, The DEAD-box RNA helicase DDX3 associates with export messenger ribonucleoproteins as well as tip-associated protein and participates in translational control. *Mol Biol Cell* **19**, 3847-3858 (2008).

97. M. Hondele *et al.*, DEAD-box ATPases are global regulators of phase-separated organelles. *Nature* **573**, 144-148 (2019).

98. E. A. Gustafson, G. M. Wessel, DEAD-box helicases: posttranslational regulation and function. *Biochem Biophys Res Commun* **395**, 1-6 (2010).

99. D. Soulat *et al.*, The DEAD-box helicase DDX3X is a critical component of the TANK-binding kinase 1-dependent innate immune response. *EMBO J* **27**, 2135-2146 (2008).

100. L. Calviello *et al.*, DDX3 depletion represses translation of mRNAs with complex 5' UTRs. *Nucleic Acids Res*, (2021).

101. G. M. Bol, M. Xie, V. Raman, DDX3, a potential target for cancer treatment. *Mol Cancer* **14**, 188 (2015).

102. T. Z. Berardini *et al.*, The Arabidopsis information resource: Making and mining the "gold standard" annotated reference plant genome. *Genesis* **53**, 474-485 (2015).

103. A. V. Klepikova, A. S. Kasianov, E. S. Gerasimov, M. D. Logacheva, A. A. Penin, A high resolution map of the Arabidopsis thaliana developmental transcriptome based on RNA-seq profiling. *Plant J* **88**, 1058-1070 (2016).

104. Y. He *et al.*, A double-edged function of DDX3, as an oncogene or tumor suppressor, in cancer progression (Review). *Oncol Rep* **39**, 883-892 (2018).

105. M. R. Heerma van Voss *et al.*, The prognostic effect of DDX3 upregulation in distant breast cancer metastases. *Clin Exp Metastasis* **34**, 85-92 (2017).

106. C. Y. Su *et al.*, DDX3 as a strongest prognosis marker and its downregulation promotes metastasis in colorectal cancer. *Oncotarget* **6**, 18602-18612 (2015).

107. J. Collemare, R. O'Connell, M.-H. Lebrun, Nonproteinaceous effectors: the terra incognita of plant-fungal interactions. *New Phytol.* **223**, 590-596 (2019).

108. J. M. Vance *et al.*, Chorea-acanthocytosis: a report of three new families and implications for genetic counselling. *Am. J. Med. Genet.* **28**, 403-410 (1987).

109. M. Nafisi *et al.*, Arabidopsis cytochrome P450 monooxygenase 71A13 catalyzes the conversion of indole-3-acetaldoxime in camalexin synthesis. *Plant Cell* **19**, 2039-2052 (2007).

110. S. B. Andersen *et al.*, The life of a dead ant: the expression of an adaptive extended phenotype. *Am. Nat.* **174**, 424-433 (2009).

111. C. de Bekker, R. A. Ohm, H. C. Evans, A. Brachmann, D. P. Hughes, Ant-infecting Ophiocordyceps genomes reveal a high diversity of potential behavioral manipulation genes and a possible major role for enterotoxins. *Sci. Rep.* **7**, 12508 (2017).

112. J. P. M. Araújo, D. P. Hughes, Zombie-ant fungi emerged from non-manipulating, beetle-infecting ancestors. *Curr. Biol.* **29**, 3735-3738.e3732 (2019).

113. T. Pusztahelyi, I. J. Holb, I. Pócsi, Secondary metabolites in fungus-plant interactions. *Front. Plant Sci.* **6**, 573 (2015).

114. J. P. Morrissey, A. E. Osbourn, Fungal resistance to plant antibiotics as a mechanism of pathogenesis. *Microbiol. Mol. Biol. Rev.* **63**, 708-724 (1999).

115. A. E. Osbourn, B. R. Clarke, P. Lunness, P. R. Scott, M. J. Daniels, An oat species lacking avenacin is susceptible to infection by Gaeumannomyces graminis var. tritici. *Physiol. Mol. Plant Pathol.* **45**, 457-467 (1994).

116. C. N. Armah *et al.*, The membrane-permeabilizing effect of avenacin A-1 involves the reorganization of bilayer cholesterol. *Biophys. J.* **76**, 281-290 (1999).

117. P. Bowyer, B. R. Clarke, P. Lunness, M. J. Daniels, A. E. Osbourn, Host range of a plant pathogenic fungus determined by a saponin detoxifying enzyme. *Science* **267**, 371-374 (1995).

118. M. Chen *et al.*, Dual targeting of DDX3 and eIF4A by the translation inhibitor rocaglamide A. *Cell Chem Biol* **28**, 475-486 e478 (2021).

119. T. Yamaguchi *et al.*, Turn-ON fluorescent affinity labeling using a small bifunctional O-nitrobenzoxadiazole unit. *Chem Sci* **5**, 1021-1029 (2014).

120. H. Mi *et al.*, Protocol Update for large-scale genome and gene function analysis with the PANTHER classification system (v.14.0). *Nat Protoc* **14**, 703-721 (2019).

121. J. L. Fox, M. MacFarlane, Targeting cell death signalling in cancer: minimising 'Collateral damage'. *Br J Cancer* **115**, 5-11 (2016).

122. L. Shen *et al.*, The fundamental role of the p53 pathway in tumor metabolism and its implication in tumor therapy. *Clin Cancer Res* **18**, 1561-1567 (2012).

123. A. Jeanes, C. J. Gottardi, A. S. Yap, Cadherins and cancer: how does cadherin dysfunction promote tumor progression? *Oncogene* **27**, 6920-6929 (2008).

124. H. Chen, H. Liu, G. Qing, Targeting oncogenic Myc as a strategy for cancer treatment. *Signal Transduct Target Ther* **3**, 5 (2018).

125. W. R. Taylor, G. R. Stark, Regulation of the G2/M transition by p53. *Oncogene* **20**, 1803-1815 (2001).

126. S. Anders, W. Huber, Differential expression analysis for sequence count data. *Genome Biol* **11**, (2010).

127. C. L. Schoch *et al.*, Finding needles in haystacks: linking scientific names, reference specimens and molecular data for Fungi. *Database* **2014**, (2014).

128. Y.-P. Xiao, T.-C. Wen, S. Hongsanan, J.-Z. U. Sun, K. D. Hyde, Introducing Ophiocordyceps thanathonensis, a new species of entomogenous fungi on ants, and a reference specimen for O. pseudolloydii. *Phytotaxa* **328**, 115-126 (2017).

129. P. Gan, N. Nakata, T. Suzuki, K. Shirasu, Markers to differentiate species of anthracnose fungi identify Colletotrichum fructicola as the predominant virulent species in strawberry plants in Chiba Prefecture of Japan. *J. Gen. Plant Pathol.* **83**, 14-22 (2017).

130. Z.-Y. Liu *et al.*, Molecular evidence for teleomorph-anamorph connections in <i.Cordyceps based on ITS-5.8S rDNA sequences. *Mycol. Res.* **106**, 1100-1108 (2002).

131. L. A. Castlebury, A. Y. Rossman, G.-H. Sung, A. S. Hyten, J. W. Spatafora, Multigene phylogeny reveals new lineage for Stachybotrys chartarum, the indoor air fungus. *Mycol. Res.* **108**, 864-872 (2004).

132. J. W. Spatafora, G. H. Sung, J. M. Sung, N. L. Hywel-Jones, J. F. White, Jr., Phylogenetic evidence for an animal pathogen origin of ergot and the grass endophytes. *Mol. Ecol.* **16**, 1701-1711 (2007).

133. G.-H. Sung *et al.*, Phylogenetic classification of Cordyceps and the clavicipitaceous fungi. *Stud. Mycol.* **57**, 5-59 (2007).

134. J. J. Luangsa-Ard, R. Ridkaew, S. Mongkolsamrit, K. Tasanathai, N. L. Hywel-Jones, Ophiocordyceps barnesii and its relationship to other melolonthid pathogens with dark stromata. *Fungal Biol.* **114**, 739-745 (2010).

135. J. J. Luangsa-Ard, R. Ridkaew, K. Tasanathai, D. Thanakitpipattana, N. Hywel-Jones, Ophiocordyceps halabalaensis: a new species of Ophiocordyceps

pathogenic to Camponotus gigas in Hala Bala Wildlife Sanctuary, Southern Thailand. *Fungal Biol.* **115**, 608-614 (2011).

136. R. M. Kepler *et al.*, New teleomorph combinations in the entomopathogenic genus Metacordyceps. *Mycologia* **104**, 182-197 (2012).

137. C. L. Schoch *et al.*, Nuclear ribosomal internal transcribed spacer (ITS) region as a universal DNA barcode marker for Fungi. *Proc. Natl. Acad. Sci. U. S. A.* **109**, 6241-6246 (2012).

138. Z.-H. Chen *et al.*, Systematic analyses of Ophiocordyceps lanpingensis sp. nov., a new species of Ophiocordyceps in China. *Microbiol. Res.* **168**, 525-532 (2013).

139. X. Hu *et al.*, Genome survey uncovers the secrets of sex and lifestyle in caterpillar fungus. *Chin. Sci. Bull.* **58**, 2846-2854 (2013).

140. T.-C. Wen *et al.*, Ophiocordyceps xuefengensis sp. nov. from larvae of Phassus nodus (Hepialidae) in Hunan Province, southern China. *Phytotaxa* **123**, 41-50 (2013).

141. C. A. Quandt *et al.*, Phylogenetic-based nomenclatural proposals for Ophiocordycipitaceae (Hypocreales) with new combinations in Tolypocladium. *IMA Fungus* **5**, 121-134 (2014).

142. S. Ban, T. Sakane, A. Nakagiri, Three new species of Ophiocordyceps and overview of anamorph types in the genus and the family Ophiocordyceptaceae. *Mycol. Prog.* **14**, (2015).

143. T. I. Sanjuan *et al.*, Five new species of entomopathogenic fungi from the Amazon and evolution of neotropical Ophiocordyceps. *Fungal Biol.* **119**, 901-916 (2015).

144. C. A. Quandt, W. Patterson, J. W. Spatafora, Harnessing the power of phylogenomics to disentangle the directionality and signatures of interkingdom host jumping in the parasitic fungal genus Tolypocladium. *Mycologia* **110**, 104-117 (2018).

145. I. Will *et al.*, Genetic underpinnings of host manipulation by Ophiocordyceps as revealed by comparative transcriptomics. *G3* **10**, 2275-2296 (2020).

146. K. Katoh, D. M. Standley, MAFFT multiple sequence alignment software version 7: improvements in performance and usability. *Mol. Biol. Evol.* **30**, 772-780 (2013).

147. S. Capella-Gutiérrez, J. M. Silla-Martínez, T. Gabaldón, trimAl: a tool for automated alignment trimming in large-scale phylogenetic analyses. *Bioinformatics* **25**, 1972-1973 (2009).

148. S. Kumar, G. Stecher, K. Tamura, MEGA7: molecular evolutionary genetics analysis version 7.0 for bigger datasets. *Mol. Biol. Evol.* **33**, 1870-1874 (2016).

149. A. Stamatakis, RAxML version 8: a tool for phylogenetic analysis and post-analysis of large phylogenies. *Bioinformatics* **30**, 1312-1313 (2014).